

1 **Augmentation of WRF-Hydro to Simulate Overland Flow- and**  
2 **Streamflow-Generated Debris Flow Susceptibility in Burn Scars**

3  
4 **Chuxuan Li<sup>1</sup>, Alexander L. Handwerker<sup>2,3</sup>, Jiali Wang<sup>4</sup>, Wei Yu<sup>5,6</sup>, Xiang Li<sup>7</sup>, Noah J.**  
5 **Finnegan<sup>8</sup>, Yingying Xie<sup>9,10</sup>, Giuseppe Buscarnera<sup>7</sup>, and Daniel E. Horton<sup>1</sup>**

6 <sup>1</sup> Department of Earth and Planetary Sciences, Northwestern University, Evanston, IL, 60208, USA

7 <sup>2</sup> Joint Institute for Regional Earth System Science and Engineering, University of California, Los Angeles,  
8 CA, 90095, USA

9 <sup>3</sup> Jet Propulsion Laboratory, California Institute of Technology, Pasadena, CA, 91109, USA

10 <sup>4</sup> Environmental Science Division, Argonne National Laboratory, Lemont, IL, 60439, USA

11 <sup>5</sup> Cooperative Institute for Research in Environmental Sciences, University of Colorado Boulder, CO,  
12 80309, USA

13 <sup>6</sup> NOAA/Global Systems Laboratory, 325 Broadway Boulder, Denver, CO, 80305-3328, USA

14 <sup>7</sup> Department of Civil and Environmental Engineering, Northwestern University, Evanston, IL, 60208, USA

15 <sup>8</sup> Department of Earth and Planetary Sciences, University of California Santa Cruz, Santa Cruz, CA, 95064,  
16 USA

17 <sup>9</sup> Program in Environmental Sciences, Northwestern University, 2145 Sheridan Road, Evanston, IL, 60208,  
18 USA

19 <sup>10</sup> Department of Biological Sciences, Purdue University, 915 W State St, West Lafayette, IN 47907, USA

20  
21 *Correspondence to:* Chuxuan Li ([chuxuanli2020@u.northwestern.edu](mailto:chuxuanli2020@u.northwestern.edu))

## 29 **Abstract**

30 In steep wildfire-burned terrains, intense rainfall can produce large runoff that can trigger highly  
31 destructive debris flows. However, the ability to accurately characterize and forecast debris-flow  
32 susceptibility in burned terrains using physics-based tools remains limited. Here, we augment the  
33 Weather Research and Forecasting Hydrological modeling system (WRF-Hydro) to simulate both  
34 overland and channelized flows and assess postfire debris flow susceptibility over a regional  
35 domain. We perform hindcast simulations using high-resolution weather radar-derived  
36 precipitation and reanalysis data to drive non-burned baseline and burn scar sensitivity  
37 experiments. Our simulations focus on January 2021 when an atmospheric river triggered  
38 numerous debris flows within a wildfire burn scar in Big Sur – one of which destroyed California’s  
39 famous Highway 1. Compared to the baseline, our burn scar simulation yields dramatic increases  
40 in total and peak discharge, and shorter lags between rainfall onset and peak discharge, consistent  
41 with streamflow observations at nearby U.S. Geological Survey (USGS) streamflow gage sites.  
42 For the 404 catchments located in the simulated burn scar area, median catchment-area normalized  
43 peak discharge increases by ~450% compared to the baseline. Catchments with anomalously high  
44 catchment-area normalized peak discharge correspond well with post-event field-based and  
45 remotely-sensed debris flow observations. We suggest that our regional post-fire debris flow  
46 susceptibility analysis demonstrates WRF-Hydro as a compelling new physics-based tool whose  
47 utility could be further extended via coupling to sediment erosion and transport models and/or  
48 ensemble-based operational weather forecasts. Given the high-fidelity performance of our  
49 augmented version of WRF-Hydro, as well as its potential usage in probabilistic hazard forecasts,  
50 we argue for its continued development and application in post-fire hydrologic and natural hazard  
51 assessments.

52

## 53 **Short Summary**

54 In January 2021 a storm triggered numerous debris flows in a wildfire burn scar in California. We  
55 use a hydrologic model to assess debris flow susceptibility in pre-fire and postfire scenarios.  
56 Compared to pre-fire conditions, postfire conditions yield dramatic increases in peak water  
57 discharge, substantially increasing debris flow susceptibility. Our work highlights the hydrologic  
58 model's utility in investigating and potentially forecasting postfire debris flows at regional scales.

## 59 **1 Introduction**

60 Following intense rainfall, areas with wildfire burn scars are more prone to flash flooding (Neary  
61 et al., 2003; Bart & Hope 2010; Bart 2016) and runoff-generated debris flows than unburned areas  
62 (Ice et al., 2004; Shakesby & Doerr, 2006; Moody et al., 2013). After wildfire, reduced tree canopy  
63 interception, decreased soil infiltration due to soil-sealing effects (Larsen et al., 2009), and  
64 increased soil water repellency – especially in hyper-arid environments (Dekker & Ritsema, 1994;

65 Doerr & Thomas, 2000; MacDonald & Huffman, 2004) – increases excess surface water, and on  
66 sloped terrains leads to overland flow (Shakesby & Doerr, 2006; Stoof et al., 2012). As water  
67 moves down hillslopes and erosion adds sediment to water-dominated flows, clear water floods  
68 can transition to turbulent and potentially destructive debris flows (Meyer & Wells, 1997; Cannon  
69 et al., 2001, 2003; Santi et al., 2008). In contrast to debris flows initiated by shallow landslides,  
70 this rainfall-runoff process has been identified as the major cause for postfire debris flows in the  
71 western U.S. (Cannon, 2001; Cannon et al., 2003, 2008; Kean et al., 2011; Parise & Cannon, 2012;  
72 Nyman et al., 2015) and in other regions that are particularly susceptible to wildfires and  
73 subsequent heavy precipitation (Bisson et al., 2005; Mitsopoulos & Mironidis, 2006; Rosso et al.,  
74 2007; Parise & Cannon, 2008, 2009).

75 On the U.S. west coast, atmospheric rivers (ARs) are the dominant synoptic weather systems  
76 responsible for producing postfire debris flows (Barth et al., 2017; Oakley et al., 2017, 2018;  
77 Young et al., 2017). ARs are long filament-like bands of elevated water vapor within the lower  
78 troposphere that often form over ocean basins. They are responsible for over 90% of poleward  
79 water vapor transport (Zhu & Newell, 1998) and often result in heavy precipitation upon landfall,  
80 particularly with orographic uplift (Ralph et al., 2004; Neiman et al., 2008). It is reported that 30–  
81 50% of annual precipitation and 60%–100% of extreme precipitation along the U.S. west coast is  
82 the result of ARs (Collow et al., 2020; Eldardiry et al., 2019; Hecht & Cordeira, 2017). In  
83 California, anthropogenic climate change is projected to increase AR intensity (Huang et al.,  
84 2020a, 2020b), increase the intensity and frequency of wet-season precipitation (Polade et al.,  
85 2017; Swain et al., 2018), increase wildfire potential (Brown et al., 2020; Swain 2021), and extend  
86 the wildfire season (Goss et al., 2020). As such, the occurrence and intensity of postfire debris  
87 flows are likely to increase as the effects of anthropogenic climate change persist (Cannon &  
88 DeGraff, 2009; Kean & Staley, 2021; Oakley 2021).

89 Due to this increasing threat, the development of tools to assess postfire debris flow susceptibility  
90 and hazards is critical. However, due to long-standing terminology ambiguity in the natural hazard  
91 community (Reichenbach et al., 2018), we first begin with a definition of terms. In this study we  
92 demonstrate the use of a new physics-based tool to map postfire debris flow susceptibility at  
93 regional scales. We follow the guidance of [Reichenbach et al., (2018) & references therein] and  
94 define *susceptibility* as the likelihood of debris flow occurrence in an area, and *hazard* as the  
95 probability of debris flow occurrence of a given magnitude within a specified area and period of  
96 time. In other words, debris flow susceptibility neither simulates debris flow dynamics such as  
97 initiation nor estimates debris flow size or considers the timing or frequency of the debris flow  
98 occurrence. Rather, it focuses on locating areas prone to debris flows considering local  
99 environmental factors (Brabb 1985; Guzzetti et al., 2005).

100 Heuristic, deterministic, statistical approaches, and coupled deterministic and statistical models  
101 have previously been employed to assess landslide susceptibility (Dahal et al., 2008; Regmi et al.,  
102 2010; Park et al., 2016; Reichenbach et al., 2018). For postfire debris flow susceptibility or hazard  
103 assessment, however, the use of deterministic models is limited. In contrast, statistical approaches

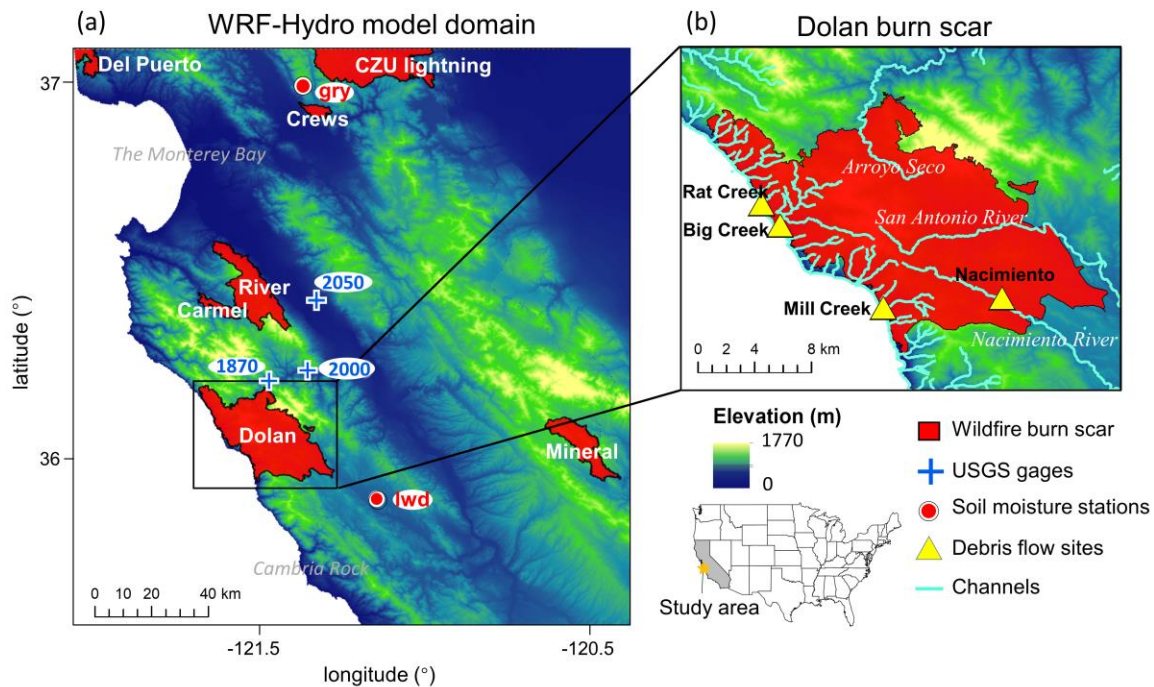
104 are commonly used in both research and operational settings (Cannon et al., 2010; Friedel 2011a,  
105 2011b; Gardner et al., 2014; Staley et al., 2016; Nikolopoulos et al., 2018; Cui et al., 2019). For  
106 example, rainfall intensity-duration (ID) thresholds are one of the simplest-to-implement and most  
107 widely used statistical methods for mapping rainfall-induced landslide susceptibility including  
108 postfire debris flows (Cannon et al., 2011; Staley et al., 2017). In addition, the U.S. Geological  
109 Survey (USGS) currently employs a statistical approach in their Emergency Assessment of  
110 Postfire Debris-flow Hazards that consists of a logistic regression model to predict the likelihood  
111 of post-wildfire debris flows (e.g., Cannon et al., 2010; Staley et al., 2016), and a multiple linear  
112 regression model to predict debris flow volumes (Gartner et al., 2014). Machine-learning  
113 techniques such as self-organizing maps, genetic programming, and a random forest algorithm  
114 have also been used to predict postfire debris flows in the western U.S. (Friedel 2011a, 2011b;  
115 Nikolopoulos et al., 2018). In general, statistical approaches are useful for identifying and  
116 characterizing relationships amongst contributing environmental factors and are widely used due  
117 to their low computational costs and the potential for rapid assessment. Despite the utility and  
118 advantages of data-driven hazard prediction approaches over regional domains, these techniques  
119 (1) do not simulate the underlying physics, (2) often require large amount of historical observation  
120 data that may not be readily available, and (3) result in models that are often only applicable to  
121 specific locales. These limitations inhibit their utility in postfire debris flow susceptibility  
122 assessment from a physics-based perspective, limit their applicability in climatological and  
123 geographic settings different than their training sites, and limit their use in non-stationary  
124 conditions (e.g., under changing climatic conditions).

125 In contrast, physics-based models that simulate spatially-explicit hydrologic and mass wastage  
126 processes are well-suited for sensitivity analyses in diverse settings. However, studies employing  
127 deterministic process-based models have tended to focus on rainfall-induced shallow landslides  
128 (Crosta & Frattini, 2003; Claessens et al., 2007) or landslide-induced debris flows (e.g., Iverson &  
129 George, 2014; George & Iverson, 2014), rather than on runoff-generated debris flows which are  
130 more common in postfire areas (Cannon et al., 2001, 2003; Santi et al., 2008). Studies that have  
131 investigated postfire hydrologic responses using physics-based models have largely focused on  
132 mechanistic studies such as short-term responses at high spatiotemporal resolutions (Rengers et  
133 al., 2016; McGuire et al., 2016, 2017) or long-term runoff responses at coarse temporal resolutions  
134 (McMichael & Hope, 2007; Rulli & Rosso, 2007) in individual catchments. For example, process-  
135 based models have employed shallow water equations to better understand the triggering (McGuire  
136 et al., 2017; Tang et al., 2019a, 2019b) and sediment transport mechanisms (McGuire et al., 2016)  
137 of postfire debris flows as well as the timing of postfire debris flows (Rengers et al., 2016). The  
138 numerical models employed by these studies are used to simulate debris flow dynamics rather than  
139 assess susceptibility over regional domains, as such they focus on individual catchments (with  
140 drainage areas of  $\sim 1 \text{ km}^2$ ) with very high spatiotemporal resolutions (Rengers et al., 2016;  
141 McGuire et al., 2016, 2017; Tang et al., 2019a, 2019b). In addition to individual catchment  
142 applications, process-based models often adopt simplifications that can limit effective prediction  
143 and hypothesis testing to overcome computational limits. For example, the kinematic runoff and

144 erosion model (KINEROS2) simplifies drainage basins into 1-dimensional channels and hillslope  
145 patches (Canfield et al., 2005; Goodrich et al., 2012; Sidman et al., 2016), and the Hydrologic  
146 Modeling System (HEC-HMS) uses an empirically-based curve number method to estimate  
147 saturation excess water (Cyzik et al., 2009), which cannot resolve infiltration excess overland  
148 flow, a critical process in burn scars (Chen et al., 2013).

149 Given the current state of debris flow susceptibility assessment and prediction in previously burned  
150 terrains, in addition to the growing influence of anthropogenic climate change on wildfire and  
151 extreme precipitation, development of physics-based susceptibility mapping tools that can be used  
152 in both hindcast investigations and forecasting applications is needed. Furthermore, due to the  
153 diverse morphology and often large spatial scales of precipitation events and their interactions with  
154 geographically distributed wildfire burn scars, development of tools that can assess susceptibility  
155 over regional domains, particularly in operational forecasting applications, is critical. Here, to  
156 advance the field of burn scar debris flow susceptibility assessment, we explore the use of the  
157 physics-based and fully-distributed Weather Research and Forecasting Hydrological modeling  
158 system version 5.1.1 (WRF-Hydro). WRF-Hydro is an open-source community model developed  
159 by the National Center for Atmospheric Research (NCAR). It is the core of the National Oceanic  
160 and Atmospheric Administration's (NOAA) National Water Model forecasting system and has  
161 been used extensively to study channelized flows over regional domains (e.g., Wang et al., 2019;  
162 Lahmers et al., 2020). Here, we modify WRF-Hydro to output high temporal resolution fine-scale  
163 (100 m) debris flow-relevant overland flow; a process computed using a fully unsteady, explicit,  
164 finite difference diffusive wave formulation. Previous efforts, employing shallow water equations,  
165 diffusive, kinematic, and diffusive-kinematic wave models, have demonstrated that water-only  
166 models can provide critical insights on runoff-driven debris flows (Arattano & Savage, 1994;  
167 Arattano & Franzi, 2010; Di Cristo et al., 2021), even in burned watersheds (Rengers et al., 2016;  
168 McGuire & Youberg, 2020).

169 To test and demonstrate the utility of WRF-Hydro in debris flow studies, we investigate the  
170 January 2021 debris flow events within the Dolan burn scar on the Big Sur coast of central  
171 California (Fig. 1a–b). We first identify multiple debris flow sites using optical and radar remote  
172 sensing data and field investigations. We then calibrate WRF-Hydro against ground-based soil  
173 moisture and streamflow observations and use it to study the effects of burn scars on debris flow  
174 hydrology and susceptibility. The paper is organized as follows. Section 2 describes the  
175 identification approach and geologic setting of debris flows. Section 3 presents a description of  
176 WRF-Hydro. Section 4 describes the simulation, calibration, and validation of WRF-Hydro.  
177 Section 5 presents the results. Section 6 discusses the results and Sect. 7 provides a conclusion.



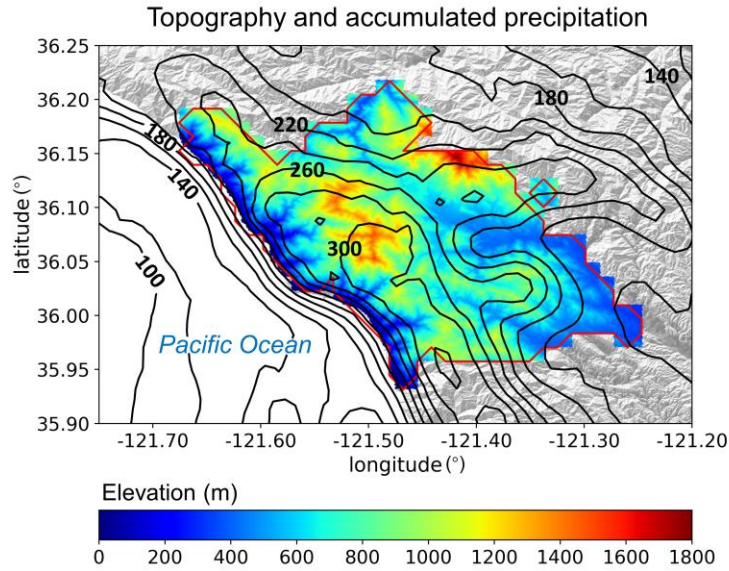
178  
 179 **Fig. 1|** WRF-Hydro model domain and Dolan burn scar. (a) WRF-Hydro model domain depicting  
 180 topography, 2020 wildfire season burn scars, and PSL soil moisture and USGS stream gage  
 181 observing sites. The black rectangle outlines (b) the Dolan burn scar inset, in which debris flow  
 182 locations and major streams are marked and labeled. The location of the study area is shown in the  
 183 embedded U.S. map with the state of California shaded in grey.

184

## 185 **2 Study domain and debris flow identification methodology**

186 The Dolan wildfire burned from August 18<sup>th</sup> till December 31<sup>st</sup>, 2020. 55% of areas within the fire  
 187 perimeter were burned at moderate-to-high severity (Burned Area Emergency Response, 2020).  
 188 After the fire, USGS Emergency Assessment of Postfire Debris-flow Hazards produced a debris  
 189 flow hazard assessment using a design storm based statistical model (USGS, 2020). On January  
 190 27–29, 2021, an AR made landfall on the Big Sur coast, bringing more than 300 mm of rainfall to  
 191 California’s Coast Ranges (Fig. 2), with a peak rainfall rate of 24 mm h<sup>-1</sup> [calculated with Multi-  
 192 Radar/Multi-Sensor System (MRMS) precipitation; Zhang et al., 2011, 2014, 2016]. During the  
 193 AR event, a section of California State Highway 1 (CA1) at Rat Creek was destroyed by a debris  
 194 flow. CA1 was subsequently closed for three months and rebuilt at a cost of ~\$11.5M (Los Angeles  
 195 Times, 2021).

196



197  
198  
199  
200  
201  
202  
203  
204

**Fig. 2|** The topography (m; shading) and MRMS accumulated precipitation (mm; contour lines) during the AR event from January 27<sup>th</sup> 00:00 to 29<sup>th</sup> 23:00 in the Dolan burn scar. Contour line interval for accumulated precipitation is 20 mm, and lines of 100, 140, 180, 220, 260, and 300 mm are labeled. The red polygon outlines the perimeter of the Dolan burn scar.

## 205 **2.1 Debris flow identification from remote sensing and field work**

206 In addition to the Rat Creek debris flow, which made national news (Los Angeles Times, 2021),  
207 we identified three other debris flows using a combination of field investigation, and open access  
208 satellite optical and synthetic aperture radar (SAR) images (Fig. 3 and Fig. B1).

209 We examined relative differences in normalized difference vegetation index (rdNDVI) defined by  
210 (Scheip & Wegmann, 2021):

$$211 \quad rdNDVI = \frac{NDVI_{post} - NDVI_{pre}}{\sqrt{NDVI_{pre} + NDVI_{post}}} \times 100 \quad (1)$$

212 where  $NDVI_{pre}$  and  $NDVI_{post}$  are the pre- and post-event normalized difference vegetation index  
213 (NDVI) images computed following:

$$214 \quad NDVI = \frac{NIR - Red}{NIR + Red} \quad (2)$$

215 where  $NIR$  is the near-infrared response and  $Red$  is the visible red response. rdNDVI was calculated  
216 from 10-m Sentinel-2 satellite data using the HazMapper v1.0 Google Earth Engine application  
217 (Scheip & Wegmann, 2021). HazMapper requires selection of an event date, pre-event window  
218 (months), post-event window (months), max cloud cover (%) and slope threshold (°). These input

219 requirements filter the number of images used to calculate the rdNDVI. We set the event date to  
220 January 27<sup>th</sup>, 2021 and used a 3 month pre- and post-event window with 0% max cloud cover and  
221 a 0° slope threshold to identify vegetation loss associated with the debris flows. We then created  
222 a binary map to highlight debris flows (and other vegetation loss) pixels above a rdNDVI  
223 vegetation loss threshold. We removed all pixels with rdNDVI > -10.

224 Lastly, we searched for debris flows (and other ground surface deformation) by examining SAR  
225 backscatter change with data acquired by the 10-m Copernicus Sentinel-1 (S1) satellites [see full  
226 description in Handwerger et al. (2022)]. We measured the change in SAR backscatter by using  
227 the log ratio approach, defined as

$$228 \quad I_{ratio} = 10 \times \log_{10}\left(\frac{\sigma_{pre}^0}{\sigma_{post}^0}\right) \quad (3)$$

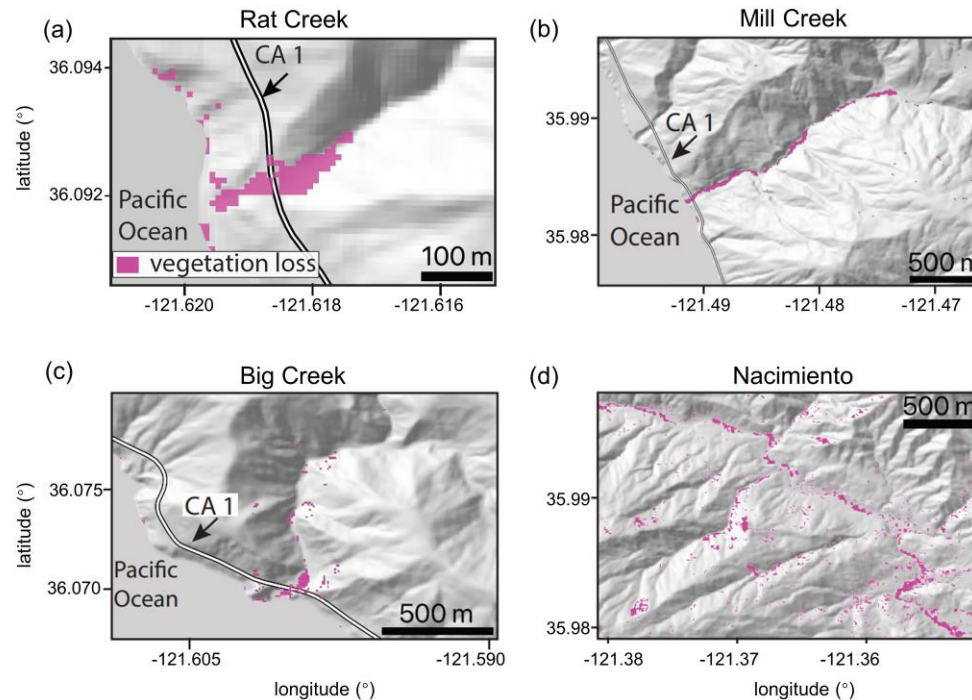
229 where  $\sigma_{pre}^0$  is a pre-event image stack (defined as the temporal median) of SAR backscatter and  
230  $\sigma_{post}^0$  is a post-event image stack. Similar to the HazMapper method, our approach requires  
231 selection of an event date, pre-event window (months), post-event window (months) and slope  
232 threshold (°). No cloud-cover threshold is needed since SAR penetrates clouds. We used a 3 month  
233 pre- and post-event window and 0° slope threshold to identify ground surface changes associated  
234 with the debris flows. We then created a binary map to highlight debris flows by removing all  
235 pixels with  $I_{ratio} < 99^{\text{th}}$  percentile value [i.e., threshold suggested by Handwerger et al. (2022)].

236 Identified debris flow source areas and deposition sites were confirmed by field investigation (N.J.  
237 Finnegan) and named after the locations where they deposited (i.e., Big Creek, Mill Creek, and  
238 Nacimiento).

239



### rdNDVI vegetation change



240

241 **Fig. 3]** Identified debris flow sites using rdNDVI vegetation change within the Dolan burn scar.  
242 We convert the rdNDVI data into a binary map by setting a threshold value, which yields only the  
243 likely debris flow locations and drape these maps over a topographic hillshade. (a)–(d) Sentinel-2  
244 rdNDVI vegetation change at (a) Rat Creek, (b) Mill Creek, (c) Big Creek, and (d) the Nacimiento  
245 River.

246

### 247 **2.2 Debris flow geologic setting**

248 According to the USGS National Elevation Dataset 30-m digital elevation model (DEM), the Rat  
249 Creek debris flow sits at the base of a 1<sup>st</sup> order catchment with a drainage area of 2.23 km<sup>2</sup>. Mill  
250 Creek, Big Creek, and Nacimiento debris flows were initiated within extremely steep, intensely  
251 burned, 1<sup>st</sup> order catchments, but were deposited in 2<sup>nd</sup>, 3<sup>rd</sup>, and 3<sup>rd</sup> Strahler stream order channels,  
252 respectively. All four debris flows were channelized. Rat Creek, Mill Creek, and Big Creek debris  
253 flow deposition sites have elevations ranging from 20–60 m, while Nacimiento debris flow  
254 deposited at an elevation of ~440 m above sea level. We calculate catchment slopes using the DEM  
255 and the slope calculation function in ArcMap. The average slope of the catchments containing Rat  
256 Creek and Mill Creek debris flow deposition sites is ~25°. The average catchment slope of Big  
257 Creek deposition site is ~28° and Nacimiento is ~21°. For debris flow source areas, the average  
258 and maximum slopes of Mill Creek are 23° and 39°, 21° and 43° for Big Creek, and 24° and 41°

259 for Nacimiento. According to the Soil Survey Geographic Database and California geologic map  
260 data, surface soils at the three coastal debris flow sites (i.e., Rat Creek, Mill Creek, and Big Creek)  
261 are texturally classified as loam with underlying Franciscan Complex sedimentary rocks of  
262 Jurassic to Cretaceous age. Soil at Nacimiento is classified as sandy loam with underlying Upper  
263 Cretaceous and Paleocene marine sedimentary rocks from the Dip Creek Formation, Asuncion  
264 Group, Shut-In Formation, Italian Flat Formation, Steve Creek Formation, and El Piojo Formation.  
265 Mill Creek, Big Creek, and Nacimiento were relatively large debris flows with runout lengths  
266 between ~2–5 km, while Rat Creek occurred in a smaller catchment and had a runout length of  
267 ~300 m. The difference in runout length and debris flow size is primarily controlled by upstream  
268 catchment size, however for the three coastal debris flow events at Rat Creek, Big Creek, and Mill  
269 Creek, also constrained by the downslope ocean. We note that there were likely more debris flows  
270 triggered during the AR event. The four debris flow events highlighted here were identified during  
271 brief post-event field excursions due to their intersection with major roadways. Given that our  
272 primary goal here is to demonstrate the utility of WRF-Hydro – a comprehensive catalogue of  
273 debris flows is beyond the scope of this study, although underway by other researchers (Cavagnaro  
274 et al., 2021).

### 275 **3 WRF-Hydro**

#### 276 **3.1 Model description**

277 WRF-Hydro is an open-source physics-based community model that simulates land surface  
278 hydrologic processes. It includes the Noah-Multiparameterization (Noah-MP) land surface model  
279 (LSM; Niu et al., 2011), terrain routing module, channel routing module, and a conceptual  
280 baseflow bucket model. The Noah-MP LSM is a 1-dimensional column model that calculates  
281 vertical energy fluxes (i.e., sensible and latent heat, net radiation), moisture (i.e., canopy  
282 interception, infiltration, infiltration excess, deep percolation), and soil thermal and moisture states  
283 on the LSM grid (1 km in our application). The infiltration excess, ponded water depth, and soil  
284 moisture are then disaggregated using a time-step weighted method (Gochis & Chen, 2003) and  
285 sent to the terrain routing module which simulates subsurface and overland flows on a finer terrain  
286 routing grid (100 m in our application). According to the mass balance, local infiltration excess,  
287 overland flow, and exfiltration from baseflow contribute to the surface head which flows into river  
288 channels if defined retention depth is exceeded. The channel routing module then calculates  
289 channelized flows assuming a trapezoidal channel shape (Fig. B2). Parameters related to the  
290 trapezoidal channel, such as channel bottom width ( $B_w$ ), Manning’s roughness coefficient ( $n$ ), and  
291 channel side slope ( $z$ ) are functions of channel stream order (Fig. B3 and Table B1). Channelized  
292 streamflow is computed at spatial resolutions ranging from 1.5 m to 100 m depending on the  
293 channel stream order (Table B1). Computed streamflow is then output on the 100-m grid.  
294 Equations used to compute infiltration excess, overland flow, and channelized flow are provided  
295 in Sect. 3.3 and 3.4.

296 By default, WRF-Hydro uses Moderate Resolution Imaging Spectroradiometer (MODIS)  
 297 Modified International Geosphere-Biosphere Program (IGBP) 20-category land cover product as  
 298 land cover (Fig. B4) and 1-km Natural Resources Conservation Service State Soil Geographic  
 299 (STATSGO) database for soil type classification (Fig. B5; Miller & White, 1998). Land surface  
 300 properties including canopy height (HVT), maximum carboxylation rate (VCMX25), and overland  
 301 flow roughness (OV\_ROUGH2D) are functions of land cover type (Table B2 & Fig. B4). Default  
 302 soil hydraulic parameters in WRF-Hydro (i.e., soil porosity, grain size distribution index, and  
 303 saturated hydraulic conductivity) are based on Cosby et al.'s (1984) soil analysis (Table B3) and  
 304 are used to map onto the STATSGO 16 soil texture types (Fig. B5).

305

### 306 **3.2 Meteorological forcing files**

307 WRF-Hydro is used in a standalone mode (i.e., it is not interactively coupled with the atmospheric  
 308 component of WRF), but rather is forced with a combination of Phase 2 North American Land  
 309 Data Assimilation System (NLDAS-2) meteorological data and MRMS radar-only quantitative  
 310 precipitation (Zhang et al., 2011, 2014, 2016). A description of the MRMS dataset and  
 311 uncertainties therein can be found in Appendix A. NLDAS-2 provides hourly forcing data  
 312 including incoming shortwave and longwave radiation, 2-m specific humidity and air temperature,  
 313 surface pressure, and 10-m wind speed at 1/8-degree spatial resolution. MRMS provides hourly  
 314 precipitation rates at 1-km resolution.

315

### 316 **3.3 Overland flow routing and output**

317 The Noah-MP LSM calculates rate of infiltration excess following Chen & Dudhia (2001):

318

$$319 \quad \frac{\partial h}{\partial t} = \frac{\partial P_d}{\partial t} \left\{ 1 - \frac{[\sum_{i=1}^4 \Delta D_i (\theta_s - \theta_i)] \left[ 1 - \exp \left( -k \frac{K_s}{K_{ref}} \delta_t \right) \right]}{P_d + [\sum_{i=1}^4 \Delta D_i (\theta_s - \theta_i)] \left[ 1 - \exp \left( -k \frac{K_s}{K_{ref}} \delta_t \right) \right]} \right\} \quad (4)$$

320

321 where  $h$  (m) is the surface water depth and  $t$  is the time.  $P_d$  (m) is the precipitation not intercepted  
 322 by the canopy;  $\Delta D_i$  (m) is the depth of soil layer  $i$ ;  $\theta_i$  is the soil moisture in soil layer  $i$ ;  $\theta_s$  is the  
 323 soil porosity;  $K_s$  ( $\text{m s}^{-1}$ ) is the saturated hydraulic conductivity;  $K_{ref}$  is  $2 \times 10^{-6} \text{ m s}^{-1}$  which  
 324 represents the saturated hydraulic conductivity of the silty-clay-loam soil texture chosen as a  
 325 reference;  $\delta_t$  (s) is the model time step; and  $k$  which is equal to 3.0 is the runoff-infiltration  
 326 partitioning parameter [the same as  $kdt_{ref}$  in Chen & Dudhia (2001)].

327

328 Noah-MP passes excess water to the terrain routing module, which simulates overland flow using  
 329 a 2-dimensional fully-unsteady, explicit, finite-difference diffusive wave equation adapted from  
 330 Julien et al. (1995) and Ogden (1997). In this application, overland flow is computed at each 6  
 331 second time step and is archived hourly at 100-m spatial resolution. The diffusive wave equation  
 332 is considered improved compared to the traditionally used kinematic wave formulation in that it  
 333 accounts for backwater effects and flow over adverse slopes. The diffusive wave formulation is  
 334 the simplified form of the Saint Venant equations, i.e., continuity and momentum equations for a  
 335 shallow water wave. The 2-dimensional continuity equation for a flood wave is:

$$336 \quad \frac{\partial h}{\partial t} + \frac{\partial q_x}{\partial x} + \frac{\partial q_y}{\partial y} = i_e \quad (5)$$

337 where  $h$  is the surface flow depth,  $q_x$  and  $q_y$  are the unit discharges in the x- and y-directions,  
 338 respectively, and  $i_e$  is the infiltration excess. Manning's equation which considers momentum loss  
 339 is used to calculate  $q$ . In the x-direction:

$$340 \quad q_x = \alpha_x h^\beta \quad (6)$$

341 Where  $\beta$  is a unit dependent coefficient equal to  $\frac{5}{3}$ , and

$$342 \quad \alpha_x = \frac{S_{fx}^{1/2}}{n_{ov}} \quad (7)$$

343 where  $n_{ov}$  is the tunable overland flow roughness coefficient. The momentum equation in the x-  
 344 direction is given by:

$$345 \quad S_{fx} = S_{ox} - \frac{\partial h}{\partial x} \quad (8)$$

346 where  $S_{fx}$  is the friction slope,  $S_{ox}$  is the terrain slope, and  $\frac{\partial h}{\partial x}$  is the change in surface flow depth  
 347 in the x-direction.

348 Off-the-shelf, WRF-Hydro does not output overland flow at terrain routing grids (100 m), however  
 349 it is computed in the background to determine channelized streamflow. One key advance made in  
 350 this work is that we modified WRF-Hydro source code to output overland flow (see the Code  
 351 availability statement for the modified source code). Overland flow depth (m) was converted to  
 352 overland discharge ( $\text{m}^3 \text{s}^{-1}$ ) by multiplying flow depth by grid cell area ( $10,000 \text{ m}^2$ ) and dividing  
 353 by the LSM time step (1 h).

354

### 355 **3.4 Channel routing**

356 If overland flow intersects grid cells identified as channel grids (2<sup>nd</sup> Strahler stream order and  
 357 above; pre-defined by the hydrologically conditioned USGS 30-m DEM), the channel routing  
 358 module routes the water as channelized streamflow using a 1-dimensional, explicit, variable time-  
 359 stepping diffusive wave formulation. In this work, the channel routing module calculates

360 streamflow at 6-s temporal resolution and spatial resolutions ranging from 1.5 m to 100 m  
 361 depending on the channel stream order (Fig. B3 and Table B1). Similarly, the continuity equation  
 362 for channel routing is given as:

$$363 \quad \frac{\partial A}{\partial t} + \frac{\partial Q}{\partial s} = q_l \quad (9)$$

364 and the momentum equation is given as:

$$365 \quad \frac{\partial Q}{\partial t} + \frac{\partial(\frac{\gamma Q^2}{A})}{\partial s} + gA \frac{\partial H}{\partial s} = -gAS_f \quad (10)$$

366 where  $s$  is the streamwise coordinate,  $H$  is water surface elevation,  $A$  is the flow cross-sectional  
 367 area calculated as  $(B_w + H z)H$  (Fig. B2),  $q_l$  is the lateral inflow rate into the channel grid,  $Q$  is  
 368 the flow rate,  $\gamma$  is a momentum correction factor,  $g$  is acceleration due to gravity, and  $S_f$  is the  
 369 friction slope computed as:

$$370 \quad S_f = \left(\frac{Q}{K}\right)^2 \quad (11)$$

371 where  $K$  is the conveyance computed from the Manning's equation:

$$372 \quad K = \frac{C_m}{n} AR^{2/3} \quad (12)$$

373 where  $n$  is the Manning's roughness coefficient,  $A$  is the channel cross-sectional area,  $R$  is the  
 374 hydraulic radius ( $A/P$ ),  $P$  is the wetted perimeter, and  $C_m$  is a dimensional constant (1.486 for  
 375 English units or 1.0 for SI units).

376

## 377 **4 Model simulation, calibration, and validation**

### 378 **4.1 Model domain**

379 The WRF-Hydro model domain spans regions in California including the Coast Ranges, Monterey  
 380 Bay, and the Central Valley, and covers several burn scars from the 2020 wildfire season (Fig. 1a).  
 381 Here we focus our analysis on the Dolan burn scar where the hazardous debris flows occurred (Fig.  
 382 1b).

383 To calibrate and validate WRF-Hydro output, we use soil moisture observations from two Physical  
 384 Sciences Laboratory (PSL) monitoring stations [i.e., Lockwood (lwd) and Gilroy (gry)] (Fig. 1a).  
 385 Due to the Mediterranean climate of California, many USGS stream gages experience low or no  
 386 flow during the dry season. In addition, many gages are under manual regulation to mitigate wet-  
 387 season flood risks and better distribute water resources. As such, it can be challenging to obtain  
 388 natural streamflow observations for model calibration. Here, three USGS stream gages [i.e.,  
 389 Arroyo Seco NR Greenfield, CA (ID 11151870), Arroyo Seco NR Soledad, CA (ID 11152000),  
 390 and Arroyo Seco BL Reliz C NR Soledad, CA (ID 11152050)] (Fig. 1a) on streams that have  
 391 measurable flows during our study period and are free of human regulation are used. These gages

392 are located downstream of the Dolan burn scar and hence are useful in calibrating the parameters  
393 associated with burn scar effects. The PSL soil moisture observations were recorded at 2-minute  
394 intervals and USGS streamflow gage data were recorded at 15-minute intervals, but we perform  
395 all observation-model comparisons at hourly-mean resolution.

396

## 397 **4.2 Baseline simulation and soil moisture calibration**

398 WRF-Hydro was initialized with National Centers for Environmental Prediction (NCEP) FNL  
399 (Final) Operational Global Analysis data and was run from January 1–31, 2021. We performed the  
400 baseline simulation by modifying WRF-Hydro default parameters (Table B3) based on a  
401 calibration using soil moisture observations from stations lwd and gry. Neither PSL station is  
402 located in a burn scar. Since the baseline simulation includes no postfire characteristics, it can also  
403 be regarded as the “pre-fire” scenario. Soil moisture at 10 cm below ground in the baseline  
404 simulation was calibrated by performing a domain-wide adjustment of soil porosity and grain size  
405 distribution index at the simulation start (Table B3). We then allowed the model to spin up from  
406 January 1–10 before using January 11–31 for validation. Using a relatively short spin-up period is  
407 justified because prior to the AR event, little rain fell on the Dolan burn scar (i.e., ~400 mm of  
408 rainfall fell from June to December 2020). As such, in the months preceding the debris flow events,  
409 soil moisture observations indicate already dry conditions prior to our 10 day spin up.

410

411 After calibration, the simulated soil moisture closely mimics ground-based PSL observations (Fig.  
412 4). Both the observed magnitude and variability are well captured, with the simulated  $\pm 1$  standard  
413 deviation envelope largely encompassing PSL observations during the AR. Model performance  
414 was evaluated using four quantitative metrics, i.e., correlation coefficient ( $r$ ), root mean square  
415 error (RMSE), mean absolute error (MAE), and Kling-Gupta efficiency (KGE; Gupta et al., 2009;  
416 Kling et al., 2012). KGE has previously been used in soil moisture calibration applications (e.g.,  
417 Lahmers et al., 2019; Vergopolan et al., 2020) and is computed as follows:

418

$$419 \quad KGE = 1 - \sqrt{(r - 1)^2 + (\alpha - 1)^2 + (\beta - 1)^2} \quad (13)$$

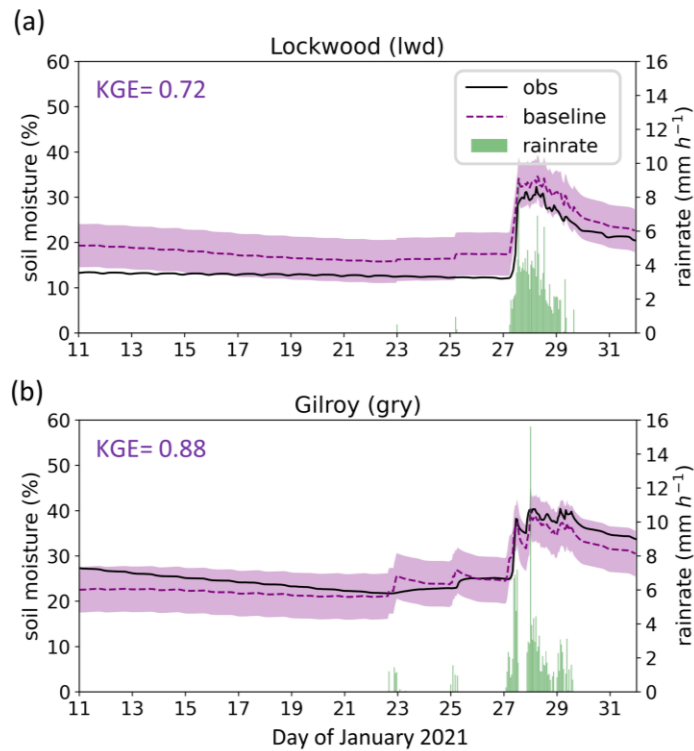
420

421 where  $r$  is the correlation coefficient between the observation and simulation,  $\alpha$  is the ratio of the  
422 standard deviation of simulation to the standard deviation of observation, and  $\beta$  is the ratio of the  
423 mean of simulation to the mean of observation. KGEs close to 1 indicate a high-level consistency  
424 between the simulation and observation, while negative KGEs indicate poor model performance  
425 (Andersson et al., 2017; Schönfelder et al., 2017).

426

427 The model’s ability to simulate soil moisture substantially improves after calibration (Fig. 4; Table  
428 1). KGE values approach 1 (0.72 at lwd and 0.88 at gry), indicating that WRF-Hydro adequately  
429 simulates the hydrologic environment and its response to meteorological changes.

MRMS precipitation, observed and simulated soil moisture



431  
 432 **Fig. 4|** Precipitation, observed and simulated soil moisture at two PSL soil moisture stations.  
 433 January 11–31, 2021 MRMS precipitation ( $\text{mm h}^{-1}$ ; green bars) and observed (%; black line) and  
 434 simulated volumetric soil moisture 10 cm below ground in the baseline simulation (%; purple  
 435 dashed line) at PSL sites (a) Lockwood (lwd) and (b) Gilroy (gry). Envelope of purple shading  
 436 depicts  $\pm 1$  standard deviation of model simulated soil moisture. KGE scores are provided at top  
 437 left for each station.

438

439

440

441 *Table 1*

442 *Evaluation metrics of simulated soil moisture and streamflow*

443

Soil moisture (Default / Baseline)				
Station	$r$	RMSE	MAE	KGE
lwd	0.97 / <u>0.98</u>	7.06 / <u>4.32</u>	5.21 / <u>4.16</u>	0.10 / <u>0.72</u>

<b>gry</b>	0.94 / 0.94	5.19 / <u>2.53</u>	11.12 / <u>2.31</u>	0.80 / <u>0.88</u>
<b>Streamflow (Baseline / Burn scar)</b>				
<b>Station</b>	<b><i>r</i></b>	<b>RMSE</b>	<b>MAE</b>	<b>NSE</b>
<b>1870</b>	0.28 / <u>0.93</u>	39.29 / <u>14.69</u>	16.05 / <u>6.14</u>	-0.17 / <u>0.84</u>
<b>2000</b>	0.26 / <u>0.86</u>	51.22 / <u>24.92</u>	20.11 / <u>10.00</u>	-0.15 / <u>0.73</u>
<b>2050</b>	0.25 / <u>0.81</u>	49.96 / <u>27.43</u>	19.64 / <u>11.65</u>	-0.38 / <u>0.53</u>

444  
445 **Table 1|** Quantitative evaluation metrics for the simulated soil moisture and streamflow when  
446 compared against observations. The metrics include the Pearson correlation coefficient (*r*), root  
447 mean square error (RMSE), and mean absolute error (MAE). In addition, the comprehensive  
448 metrics Kling-Gupta efficiency (KGE) and Nash-Sutcliffe efficiency (NSE) are used to evaluate  
449 model-simulated soil moisture and streamflow, respectively. For soil moisture, the numbers in  
450 front of “/” are calculated between the default run (i.e., uncalibrated run) and the observations,  
451 whereas the numbers following “/” are the corresponding values in the baseline simulation (the  
452 purple dashed line in Fig. 4). For streamflow, the numbers in front of “/” are computed between  
453 the baseline run (purple dashed line in Fig. 6) and the observations, while the numbers behind “/”  
454 are for burn scar simulation (red line in Fig. 6). If the model performance regarding a certain metric  
455 is enhanced in the burn scar simulation, the number after “/” is underlined.  
456

### 457 **4.3 Burn scar simulation and streamflow calibration**

458 To simulate effects of wildfire burn scars on hydrologic processes and debris flow susceptibility,  
459 we made two modifications to the baseline simulation soil moisture calibrated model configuration.  
460 First, we changed the land cover type within the burn scar perimeter to its nearest LSM analogue,  
461 i.e., “barren and sparsely vegetated”. The switch to barren land causes: (1) height of the canopy  
462 (HVT) to decrease to 0.5 m; (2) maximum rate of carboxylation at 25°C (VCMX25) to decrease  
463 to 0  $\mu\text{mol CO}_2/(\text{m}^2 \cdot \text{s})$ ; and (3) overland flow roughness coefficient (OV\_ROUGH2D) to decrease  
464 to 0.035 (Fig. 5a–c) from default values (Fig. B4 and Table B2).  
465

466 The second adjustment was to decrease soil infiltration rates within the burn scar perimeter,  
467 achieved by reducing soil saturated hydraulic conductivity (DKSAT; Fig. 5d; Scott & van Wyk,  
468 1990; Cerdà, 1998; Robichaud, 2000; Martin & Moody, 2001) from default values (Table B3).  
469 Consistent with the hydrophobicity of burned soils, we calibrate the burn scar simulation by  
470 systematically exploring a range of burn scar area saturated hydraulic conductivities (0 to  $3 \times 10^{-7}$   
471  $\text{m s}^{-1}$  with a  $5 \times 10^{-8} \text{ m s}^{-1}$  increment), with the goal of reproducing streamflow behavior similar to  
472 USGS gage observations. We found that a value of  $1.5 \times 10^{-7} \text{ m s}^{-1}$  gives the highest Nash-Sutcliffe  
473 efficiency (NSE; Nash & Sutcliffe, 1970) across all three USGS stream gages (Table 1). NSE and  
474 KGE are the two most widely used metrics for calibration and evaluation of hydrologic models.



475 The NSE has previously been used in streamflow calibration applications (e.g., Xia et al., 2012;  
476 Bitew & Gebremichael, 2011), and it is calculated as follows:

477

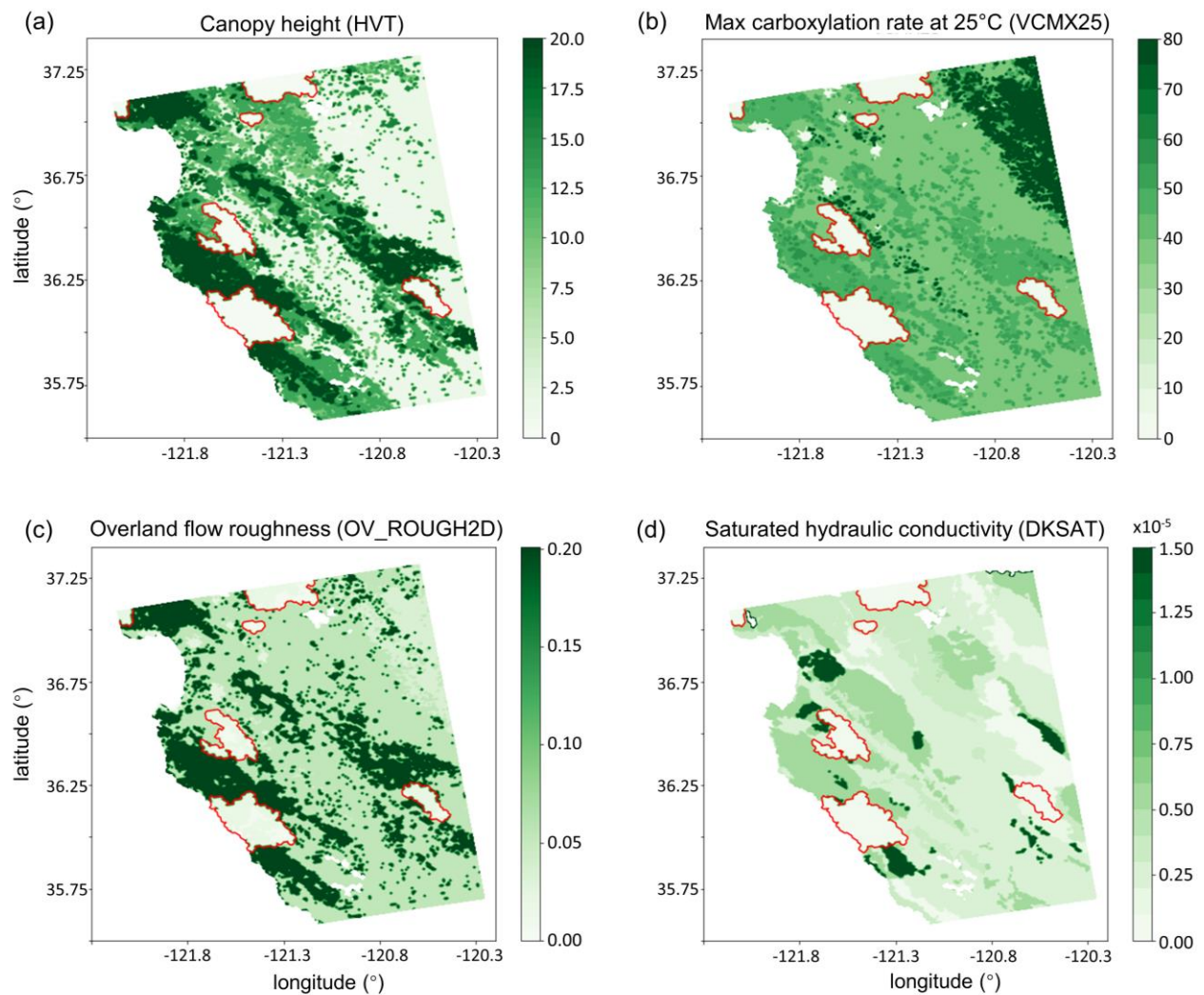
$$478 \quad NSE = 1 - \frac{\sum_{t=1}^{t=T} (Q_{sim}(t) - Q_{obs}(t))^2}{\sum_{t=1}^{t=T} (Q_{obs}(t) - \overline{Q_{obs}})^2} \quad (14)$$

479

480 where  $T$  is the length of the time series,  $Q_{sim}(t)$  and  $Q_{obs}(t)$  are the simulated and observed  
481 discharge at time  $t$ , respectively, and  $\overline{Q_{obs}}$  is the mean observed discharge. By definition, NSEs of  
482 1 indicate perfect correspondence between the simulated and observed streamflow. Positive NSEs  
483 indicate that the model streamflow has a greater explanatory power than the mean of the  
484 observations, whereas negative NSEs represent poor model performance (Moriasi et al., 2007;  
485 Schafli & Gupta, 2007). When burn scar characteristics are included, evaluation metrics including  
486  $r$ , RMSE, and MAE all improve, while NSEs increase from negative values in the baseline to 0.84,  
487 0.73, and 0.53 at gages 1870, 2000, and 2050, respectively. Higher correlation and NSE scores  
488 and lower errors indicate the above mentioned burn scar parameter changes improve the model's  
489 ability to simulate streamflow observations downstream of the burn scar (Table 1).

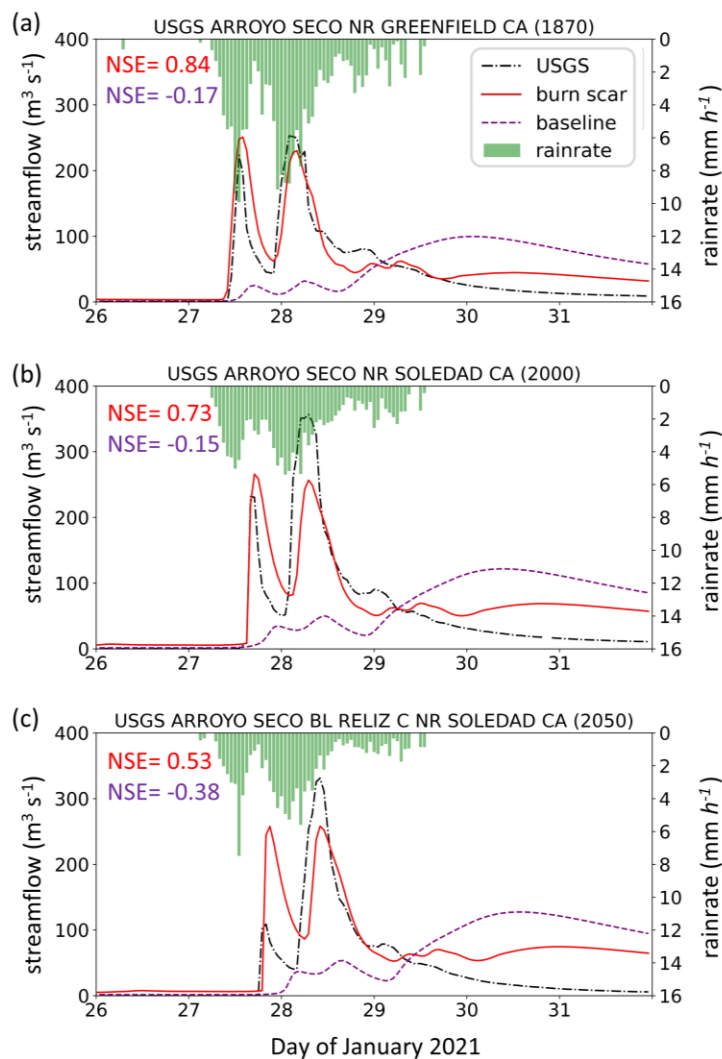
490

## Parameter changes accounting for burn scar characteristics



491  
492 **Fig. 5]** Parameter setting in the WRF-Hydro burn scar simulation. (a) The height of the canopy  
493 (HVT; m; shading), (b) maximum rate of carboxylation at 25°C (VCMX25;  $\mu\text{mol CO}_2/(\text{m}^2 \cdot \text{s})$ ;  
494 shading), (c) overland flow roughness coefficient (OV\_ROUGH2D; shading), and (d) saturated  
495 hydraulic conductivity (DKSAT;  $\text{m s}^{-1}$ ; shading) in the burn scar simulation.

MRMS precipitation, observed and simulated streamflow



496  
 497 **Fig. 6** Precipitation, observed and simulated streamflow at three USGS stream gages. January 26–  
 498 31, 2021 MRMS precipitation ( $\text{mm h}^{-1}$ ; green bars), observed ( $\text{m}^3 \text{s}^{-1}$ ; black dash dotted line) and  
 499 simulated streamflow in baseline simulation ( $\text{m}^3 \text{s}^{-1}$ ; purple dashed line) and burn scar simulation  
 500 ( $\text{m}^3 \text{s}^{-1}$ ; red line) at (a) Arroyo Seco NR Greenfield, CA (ID 11151870), (b) Arroyo Seco NR  
 501 Soledad, CA (ID 11152000), and (c) Arroyo Seco BL Reliz C NR Soledad, CA (ID 11152050).  
 502 NSE scores for baseline (purple) and burn scar simulations (red) are shown at top left.  
 503

## 504 **5 Results**

### 505 **5.1 Hydrologic response due to burn scar incorporation**

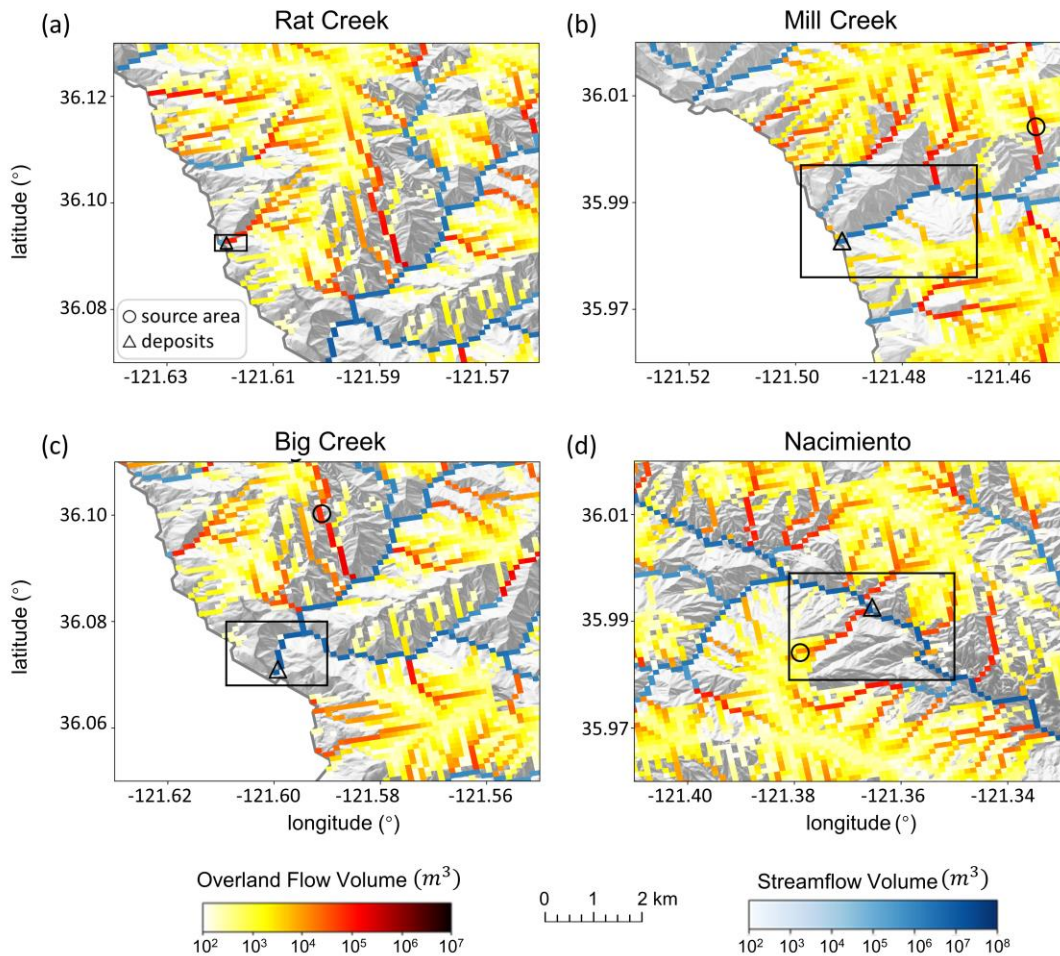
506 The pre-fire baseline simulation fails to capture the hydrologic behavior observed at the USGS  
507 gages located within the burn scar (Fig. 6). Incorporation of burn scar characteristics substantially  
508 alters the hydrologic response of the model and provides much higher fidelity streamflow  
509 simulations (Fig. 6). Observed hydrographs are characterized by two early streamflow peaks  
510 related to two precipitation bursts on January 27<sup>th</sup> and 28<sup>th</sup>. Our burn scar simulation captures this  
511 behavior, while the baseline simulation streamflow peaks just once, with a lower magnitude and  
512 an ~3-day lag after peak precipitation (Fig. 6). The steep rising limbs and high magnitude discharge  
513 peaks of the burn scar hydrograph are indicative of flash flooding. Compared with the pre-fire  
514 baseline scenario, the burn scar's barren land and low infiltration rate substantially accelerate  
515 drainage rates and increase discharge volume into stream channels.

516

### 517 **5.2 Hydrologic response at four debris flow sites**

518 Mill Creek, Big Creek, and Nacimiento deposits are located in channels of 2<sup>nd</sup> Strahler stream  
519 order or above so they are simulated as channelized streamflow in our WRF-Hydro simulations.  
520 Due to its low stream order (1<sup>st</sup> Strahler stream order), Rat Creek is modeled entirely as overland  
521 flow in our WRF-Hydro simulations. At the four debris flow sites, we use three metrics to  
522 characterize hydrologic anomalies: (1) accumulated runoff volume, (2) peak discharge, and (3)  
523 time to peak discharge. Fig. 7 depicts accumulated channelized discharge volume (blue shading)  
524 and accumulated overland discharge volume (yellow-red shading) from January 27<sup>th</sup> 00:00 to 28<sup>th</sup>  
525 12:00 near the four debris flow sites in the burn scar simulation. Accumulation time period is  
526 chosen such that it covers the first two runoff surges in the simulated hydrographs which are likely  
527 associated with debris flows (Fig. 8) given that nearly concurrent peak rainfall intensity and peak  
528 discharge is a signature characteristic of debris flows (Kean et al., 2011). Runoff volume is on the  
529 order of  $10^4 \text{ m}^3$  at Rat Creek and  $10^6 \text{ m}^3$  at the other three sites.

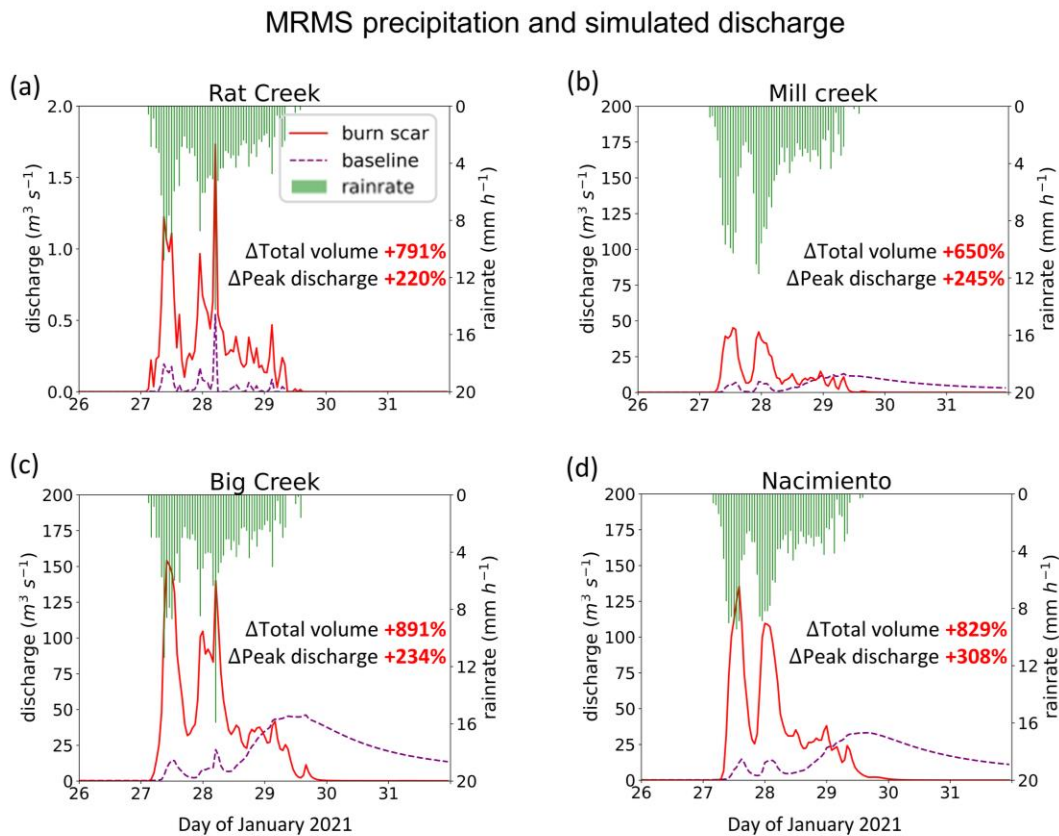
### Simulated overland flow and streamflow in burn scar simulation



530  
 531 **Fig. 7** | WRF-Hydro simulated overland flow and streamflow in the burn scar simulation. (a)–(d)  
 532 Total volume of accumulated overland flow ( $m^3$ ; yellow-red shading) and streamflow ( $m^3$ ; blue  
 533 shading) between January 27<sup>th</sup> 00:00 and 28<sup>th</sup> 12:00 at four debris flow sites draped over a hillshade  
 534 of topography. Black rectangles correspond to domains in Fig. 3a–d. Black circles and triangles  
 535 indicate debris flow source areas and deposits, respectively.

536  
 537  
 538 Dramatic hydrographic changes after inclusion of burn scar characteristics are simulated at debris  
 539 flow source areas (Fig. B6 and Table B4) and deposition sites (Fig. 8 and Table 2). Here, to  
 540 emphasize the high susceptibility downstream, our analysis is focused on debris flow deposits. At  
 541 Rat Creek, where a section of CA1 collapsed, the magnitude of discharge substantially increases,  
 542 and overland flow surges are concurrent with rainfall bursts (Fig. 8a). Total discharge accumulated  
 543 during the AR event increases approximately eight-fold (791%), and peak discharge more than

544 triples compared to the baseline simulation (Fig. 8a and Table 2). At Mill Creek, Big Creek, and  
 545 Nacimiento, baseline hydrographs are characterized by less variability, muted responses to two  
 546 early precipitation bursts, and a delayed third discharge peak that does not occur until ~3 days after  
 547 AR passage (Fig. 8b–d). Maximum discharge peaks in the baseline hydrographs lag those in the  
 548 burn scar simulation by ~2 days (Fig. 8b–d; Table 2). In the burn scar simulation, total volume  
 549 substantially increases at the three channelized sites – total volume increases ~650% at Mill Creek,  
 550 ~891% at Big Creek, and ~829% at Nacimiento (Fig. 8b–d and Table 2), and the absolute increase  
 551 in volume is on the order of  $10^6 \text{ m}^3$  (Table 2). Peak discharge more than triples at Mill Creek and  
 552 Big Creek and more than quadruples at Nacimiento. Additionally, response times of the peak in  
 553 discharge to the peak in precipitation decrease to less than an hour, highlighting the simulated  
 554 flashiness of the burned catchments.  
 555



556  
 557

558 **Fig. 8|** WRF-Hydro simulated discharge time-series at four debris flow deposition locations. (a)–  
 559 (d) MRMS precipitation ( $\text{mm h}^{-1}$ ; green bars) and simulated discharge time-series for January 26<sup>th</sup>  
 560 00:00 to 31<sup>st</sup> 23:00 at (a) Rat Creek, (b) Mill Creek, (c) Big Creek, and (d) Nacimiento deposition  
 561 locations (black triangles in Fig. 7a–d) in baseline simulation ( $\text{m}^3 \text{ s}^{-1}$ ; purple dashed line) and burn  
 562 scar simulation ( $\text{m}^3 \text{ s}^{-1}$ ; red line).



563  
564  
565  
566

*Table 2*  
*The total runoff volume, peak discharge, and peak timing at debris-flow deposits*

Site name	Baseline simulation			Burn scar simulation			
	Total volume (m <sup>3</sup> )	Peak discharge (m <sup>3</sup> s <sup>-1</sup> )	Highest peak timing	Total volume (m <sup>3</sup> )	Peak discharge (m <sup>3</sup> s <sup>-1</sup> )	1 <sup>st</sup> Peak timing	2 <sup>nd</sup> Peak timing
<b>Rat Creek</b>	6,897	0.54	28 <sup>th</sup> 05:00	61,425 (+791%)	1.73 (+220%)	27 <sup>th</sup> 09:00	28 <sup>th</sup> 05:00
<b>Mill Creek</b>	312,925	13.10	29 <sup>th</sup> 08:00	2,347,457 (+650%)	45.21 (+245%)	27 <sup>th</sup> 13:00	27 <sup>th</sup> 23:00
<b>Big Creek</b>	842,808	46.10	29 <sup>th</sup> 16:00	8,354,095 (+891%)	154.10 (+234%)	27 <sup>th</sup> 10:00	28 <sup>th</sup> 05:00
<b>Nacimiento</b>	743,531	33.15	29 <sup>th</sup> 16:00	6,904,706 (+829%)	135.41 (+308%)	27 <sup>th</sup> 14:00	28 <sup>th</sup> 00:00

567  
568  
569  
570  
571  
572  
573  
574

**Table 2**| The total runoff volume, peak discharge, and peak timing in the baseline and burn scar simulations from January 27<sup>th</sup> 00:00 to 31<sup>st</sup> 23:00 at deposition sites of Rat Creek, Mill Creek, Big Creek, and Nacimiento debris flows (black triangles in Fig. 7a–d). The peak timing shown in the baseline simulation is for the highest peak. The percent change of the total volume and peak discharge in the burn scar simulation relative to the baseline simulation are shown in parentheses.

### 5.3 Debris flow susceptibility assessment for the Dolan burn scar

Since high magnitude runoff is often the cause and precursor of runoff-generated debris flows in burned areas (Cannon et al., 2003, 2008; Rengers et al., 2016), we use peak discharge of overland flow and streamflow to assess runoff-generated debris flow susceptibility under pre-fire (i.e., baseline; Fig. 9a&d) and postfire (i.e., burn scar simulation; Fig. 9b&e) conditions [we conduct similar analyses using accumulated discharge volume in Figs. B7–9 and Table B5 in Appendix B]. We assess changes at both stream and catchment levels and use the difference between burn scar and baseline simulations to assess added debris flow susceptibility (Fig. 9c&f). Consistent with the increasing erosive and entrainment power associated with increasing discharge, our debris flow susceptibility increases as peak discharge increases. To reduce the effects of catchment size on the peak discharge-based susceptibility levels, we normalize a catchment’s discharge by the area of the catchment (Leopold et al., 1964; McCormick et al., 2009; Fig. 9d–f). Non-normalized catchment susceptibility maps are also provided (Fig. B10).

588

589 In the pre-fire baseline simulation, the AR-induced precipitation produces lower debris flow  
590 susceptibility over most of the domain, but elevated susceptibility along stream channels (Fig. 9a).  
591 We note no substantial differences between areas in or out of the burn scar. In the burn scar  
592 simulation, debris flow susceptibility levels increase across the Dolan burn scar and along channels  
593 outside but downstream of the burn scar (Fig. 9b–c). The peak discharge near Rat Creek, Big Creek,  
594 Mill Creek, and Nacimiento more than triples (Table 2 & Fig. 9a–c). Within the burn scar,  
595 susceptibility along major stream channels, such as the Nacimiento River and San Antonio River  
596 increase. Outside the burn scar, susceptibility levels along river channels downstream of the burn  
597 scar, such as the Arroyo Seco River, also increase (Fig. 9c).

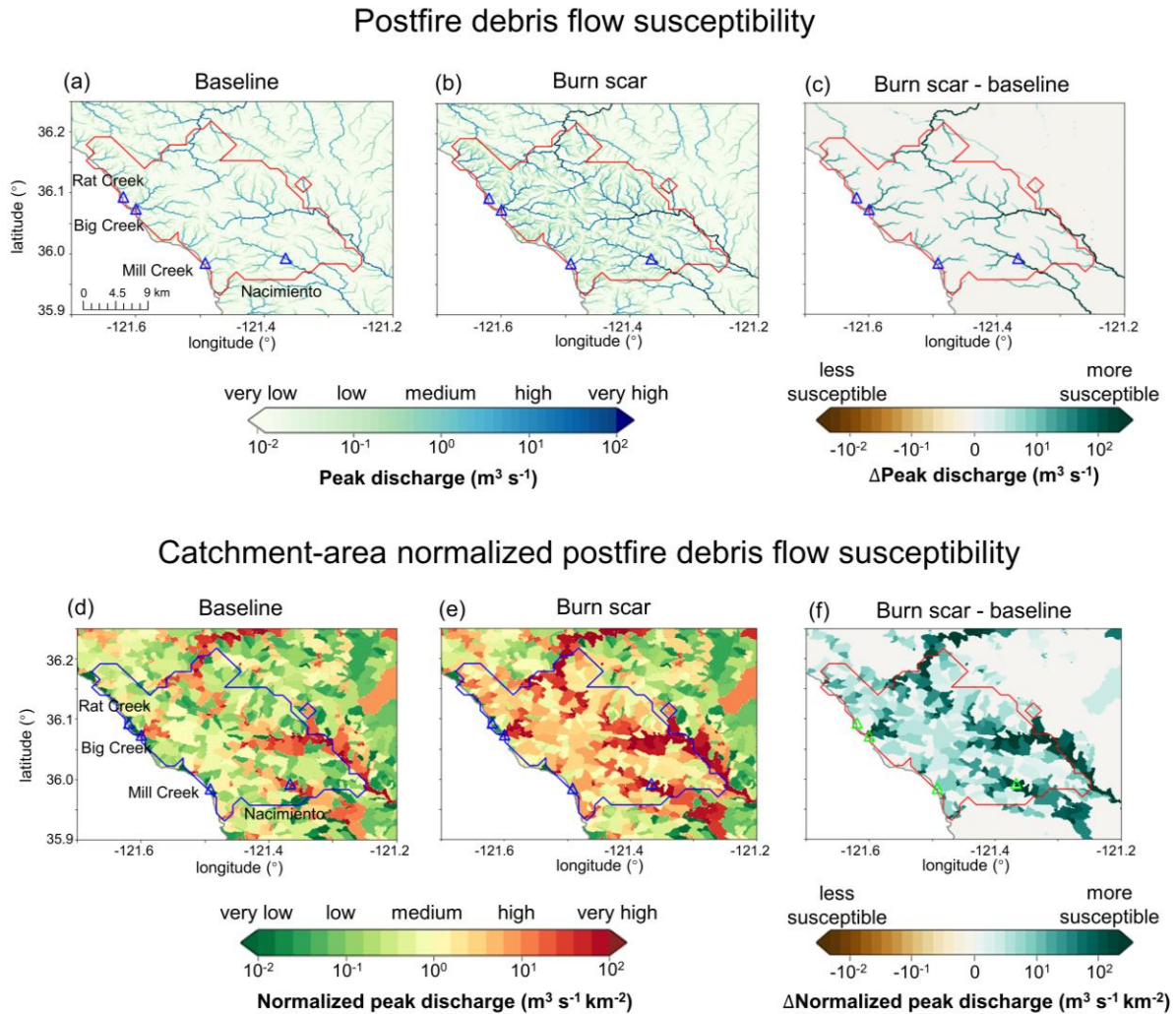
598  
599 At the catchment level, debris flow susceptibility is assessed using peak discharge normalized by  
600 catchment areas at the outlet of each catchment between January 27<sup>th</sup> 00:00 to 28<sup>th</sup> 12:00 (Fig. 9d–  
601 f). The catchment-area normalized peak discharge is classified into five categories based on equal  
602 intervals on log<sub>10</sub> scale. The susceptibility categorization follows: “very low” ( $\sim 10^{-2} \text{ m}^3 \text{ s}^{-1} \text{ km}^{-2}$ ),  
603 “low” ( $\sim 10^{-1} \text{ m}^3 \text{ s}^{-1} \text{ km}^{-2}$ ), “medium” ( $\sim 10^0 \text{ m}^3 \text{ s}^{-1} \text{ km}^{-2}$ ), “high” ( $\sim 10^1 \text{ m}^3 \text{ s}^{-1} \text{ km}^{-2}$ ), and “very high”  
604 ( $\sim 10^2 \text{ m}^3 \text{ s}^{-1} \text{ km}^{-2}$ ). In the baseline simulation, majority of catchments are subject to low or very  
605 low debris flow susceptibility with normalized peak discharge less than  $1 \text{ m}^3 \text{ s}^{-1} \text{ km}^{-2}$  (Fig. 9d). In  
606 the burn scar simulation, about half of the catchments within the Dolan burn scar have medium  
607 susceptibility or above, and about 1/4 of basins are subject to high to very high debris flow  
608 susceptibility (Fig. 9e and Table 3). The additional debris flow susceptibility brought about by the  
609 inclusion of wildfire burn scar characteristics is substantial (Fig. 9f).

610  
611 To summarize changes in debris flow susceptibility as a result of including burn scar  
612 characteristics in WRF-Hydro simulations, we create distributions of pre-fire baseline and burn  
613 scar catchment-area normalized peak discharge from the 404 catchments located within the Dolan  
614 burn scar perimeter (Fig. 10). After incorporating burn scar characteristics, the full distribution  
615 shifts to the right, indicating increased susceptibility levels – a shift considered robust by a  
616 Student’s t-test ( $p$  value:  $5.3\text{E-}23$ ). A quantitative assessment of this shift indicates that both the  
617 mean and the standard deviation of catchment area normalized peak discharge increase by more  
618 than 300% (Table 3). We also assess shifts at a range of distribution percentiles: 5P: 375%, 25P:  
619 500%, 50P: 447%, 75P: 341%, and 95P: 366% (Table 3). In the burn scar simulation, more than  
620 half of catchments have normalized peak discharge  $> 10^0 \text{ m}^3 \text{ s}^{-1} \text{ km}^{-2}$  (i.e., medium susceptibility)  
621 and about 1/4 of catchments have normalized peak discharge  $> 10^1 \text{ m}^3 \text{ s}^{-1} \text{ km}^{-2}$  (i.e., high  
622 susceptibility) – values that correspond to the 70P and 90P of the baseline simulation, respectively.  
623 Disproportionate shifting of the distribution suggests that debris flow susceptibility increases non-  
624 linearly under simulated burn scar conditions.

625 Our catchment-area normalized peak discharge-based susceptibility assessment also indicates that  
626 the catchments containing Mill Creek, Big Creek, and Nacimiento have high or very high  
627 susceptibility (Fig. 9d–f), consistent with our (limited) debris flow observations. Other areas with



628 elevated susceptibility include catchments containing the Arroyo Seco and San Antonio Rivers.  
 629 Beyond the burn scar perimeter, effects of fire expand to adjacent and downstream catchments,  
 630 and some drainage basins along the Arroyo Seco and Nacimiento Rivers are simulated to have  
 631 very high susceptibility, i.e., normalized peak discharge exceeds  $10^2 \text{ m}^3 \text{ s}^{-1} \text{ km}^{-2}$  (Fig. 9e&f).  
 632



633  
 634  
 635 **Fig. 9|** Peak discharge-based postfire debris flow susceptibility. Peak discharge at individual  
 636 stream level for the (a) baseline, (b) burn scar, and (c) difference between burn scar and  
 637 baseline simulations from January 27th 00:00 to 28th 12:00 ( $\text{m}^3 \text{ s}^{-1}$ ). (d)–(f) Normalized peak  
 638 discharge by catchment area at catchment level ( $\text{m}^3 \text{ s}^{-1} \text{ km}^{-2}$ ; shading). For each catchment,  
 639 the peak discharge is the maximum discharge rate at the catchment outlet from January 27<sup>th</sup>  
 640 00:00 to 28<sup>th</sup> 12:00 divided by catchment area. Triangles stand for debris flow deposition  
 641 locations and are annotated in (a) and (d). We conduct similar analyses using accumulated  
 642 discharge volume in Fig. B7 in Appendix B.

643  
 644  
 645  
 646  
 647  
 648

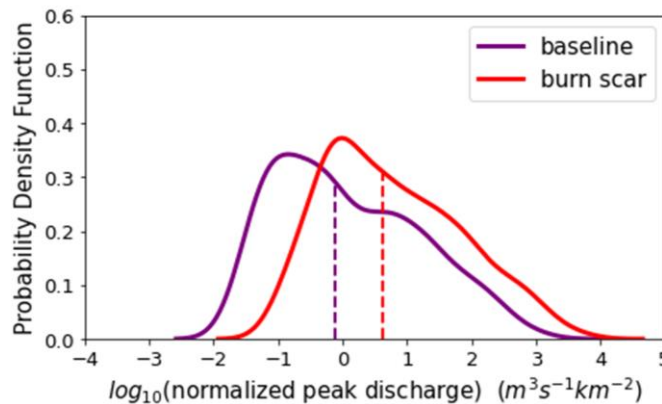
*Table 3*  
*Statistics of catchment area-normalized peak discharge in baseline and burn scar simulations*

	mean	std	5P	25P	50P	75P	95P
<b>Baseline simulation</b> ( $m^3 s^{-1} km^{-2}$ )	25.88	$\pm 95.71$	0.04	0.14	0.76	8.21	129.54
<b>Burn scar simulation</b> ( $m^3 s^{-1} km^{-2}$ )	110.80	$\pm 423.82$	0.19	0.84	4.16	36.21	603.15
<b>Relative percent change</b>	328%	343%	375%	500%	447%	341%	366%

649 **Table 3**| Statistics, including the mean, standard deviation (std), 5P, 25P, 50P, 75P, and 95P, of  
 650 the catchment-area normalized peak discharge for all the 404 basins within the Dolan burn scar in  
 651 the baseline and burn scar simulation and their relative percent changes. We conduct similar  
 652 analyses using accumulated discharge volume in Table B5 in Appendix B.

653

Distribution of catchment-area normalized peak discharge



654

655 **Fig. 10**| Distributions of peak discharge at the outlet of the 404 catchments normalized by upstream  
 656 catchment areas within Dolan burn scar in the baseline simulation (purple line) and in the burn

657 scar simulation (red line). Dashed vertical lines indicate median values. We conduct similar  
658 analyses using accumulated discharge volume in Fig. B8 in Appendix B.

659

## 660 **6 Discussion**

661 Given the historic and growing frequency of wildfires in the western U.S. (Williams et al., 2019;  
662 Goss et al., 2020; Swain 2021) and globally (Flannigan et al., 2013; Jolly et al., 2015), developing  
663 tools to investigate, better understand, and potentially predict changes in burn scar hydrology and  
664 natural hazards at regional scales is critical. Here, we demonstrate the first use of WRF-Hydro to  
665 simulate the susceptibility of a burn scar to postfire debris flows during a landfalling AR. We  
666 augmented the default version of WRF-Hydro to output overland flow and to replicate burn scar  
667 behavior by adjusting vegetation type and infiltration rate parameters. WRF-Hydro simulations  
668 were validated against PSL soil moisture and USGS streamflow observations before we used  
669 simulated peak discharge of streamflow and overland flow to characterize debris flow  
670 susceptibility. A comparison between baseline and burn scar simulations demonstrated that  
671 changes in hydraulic properties of burned areas causes drastic changes in surface flows, including  
672 faster discharge response times, and greater peak discharge and total volumes, consistent with  
673 findings from previous postfire hydrology studies (Anderson et al., 1976; Scott, 1993; Meixner &  
674 Wohlgemuth, 2003; Kean et al., 2011; Kinoshita & Hogue, 2015; Brunkal & Santi, 2016; Williams  
675 et al., 2022). At the catchment level, for the 404 catchments located within the Dolan burn scar,  
676 median catchment area-normalized peak discharge increases by ~450% relative to the baseline. In  
677 addition, Mill Creek, Big Creek, and Nacimiento basins were simulated to have high-to-very high  
678 debris flow susceptibility, corresponding well with identified debris flow occurrences.

679  
680 Despite methodological differences, our debris flow susceptibility map for this AR event is  
681 generally consistent with the USGS' postfire, pre-AR, design-storm-based preliminary hazard  
682 assessment (USGS, 2020). As described above, USGS preliminary hazard assessments use logistic  
683 regression models to estimate the likelihood of debris flow occurrence and multivariate linear  
684 regression models to estimate debris flow volumes. The USGS empirical approach is trained on  
685 historical western U.S. debris flow occurrence and magnitude data and incorporates burn scar soil  
686 erodibility and burn severity data (Cannon et al., 2010; Gartner et al., 2014; Staley et al., 2016).  
687 For precipitation, the USGS assessment utilizes a design storm approach that assumes 1–5 year  
688 return interval magnitude precipitation falls uniformly over a region/burn scar (USGS, 2020). For  
689 the Dolan burn scar, both assessments find that large stream channels had relatively higher  
690 susceptibility than small streams or overland areas. However, a close comparison of the two maps  
691 reveals differences in spatial distribution of hazardous catchments. In the USGS assessment,  
692 higher likelihood is predicted north and southeast of the burn scar, whereas in our assessment the  
693 highest susceptibility occurs along major stream channels. We hypothesize that USGS-assessed  
694 areas of higher hazard potential are related to their use of spatially uniform design-storm

695 precipitation (see Fig. 2 for MRMS precipitation footprint) and burn severity data (Burned Area  
696 Emergency Response, 2020).

697  
698 Comparison with the USGS hazard assessment framework suggests room for improvement in  
699 WRF-Hydro-based assessments (i.e., inclusion of burn severity and soil erodibility data), but also  
700 highlights the potential utility of working with spatially-distributed and time-varying precipitation.  
701 However, this also means the accuracy of WRF-Hydro predictions depends on the accuracy of  
702 precipitation forcing, and in our hindcast application, MRMS precipitation data (Appendix A).  
703 Accordingly, our WRF-Hydro-based assessment could benefit from precipitation products  
704 mosaiced from various sources to constrain precipitation-based uncertainties (e.g., gauge-  
705 corrected and/or Mountain Mapper MRMS), although the long processing time of these datasets  
706 inhibits timely post-event assessments.

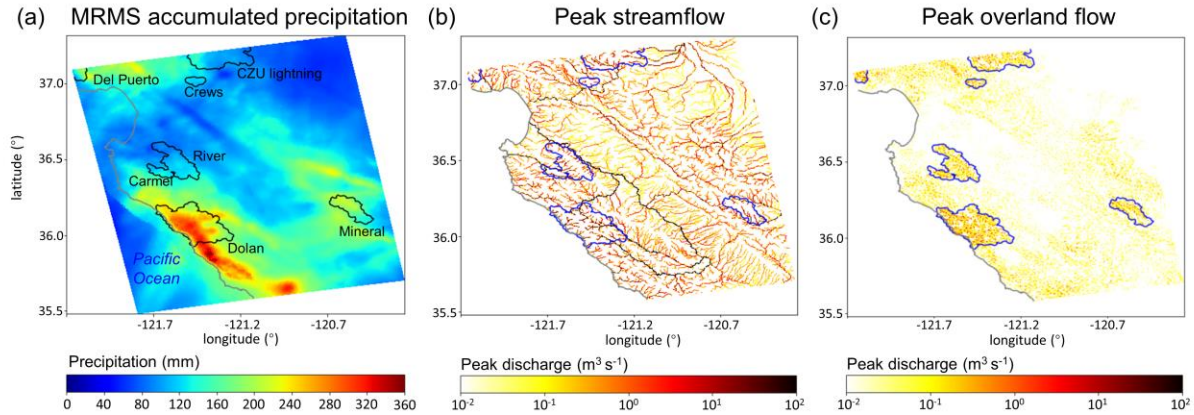
707 In addition to the above results focused primarily on the Dolan burn scar, a key feature of WRF-  
708 Hydro is its ability to simulate the land surface hydrology of expansive geographic domains, e.g.,  
709 NOAA runs the National Water Model over the entire continental U.S. Development of tools  
710 capable of regional susceptibility assessments is crucial, particularly in a wildfire-prone region  
711 like California, due to the large spatial scale, diverse morphology, and often tight spatial gradients  
712 of precipitation events and their interactions with geographically widespread wildfire burn scars.  
713 For example, landfalling ARs are often long (1000s of km) filament-like systems with  
714 heterogeneous intensity gradients along their length. As a demonstration of wide geographic  
715 applicability, we assess susceptibility over our full model domain which includes more than 10,000  
716 catchments and a number of 2020 wildfire burn scars in addition to the Dolan burn scar (Fig 11).  
717 The domain-wide analysis reveals elevated peak discharge, i.e., elevated susceptibility, in areas of  
718 high precipitation and in burned terrains (Figs. 11a–c). We highlight channelized and catchment-  
719 area normalized debris flow susceptibility in non-Dolan burn scar sites in Figs. 11d–g. In an  
720 operational forecast context, the ability to simulate landslide and debris flow susceptibilities and  
721 hazards over numerous catchments at meteorologically appropriate scales represents a step-change  
722 in the field. We argue that our demonstration of WRF-Hydro’s debris flow susceptibility hindcast

723 capabilities should motivate further exploration and development for potential use in operational  
 724 hazard forecasting.

725

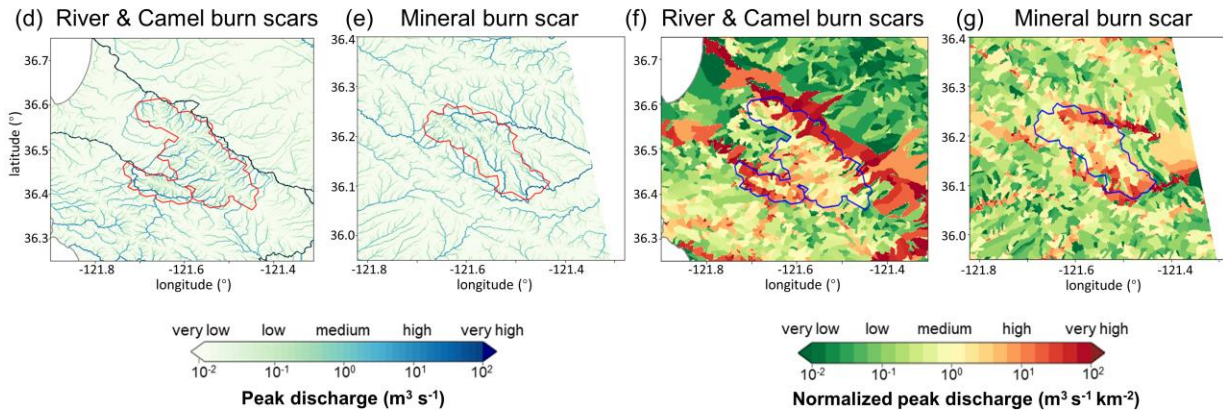
726

MRMS precipitation & peak discharge in burn scar simulation



Postfire debris flow susceptibility

Catchment-area normalized postfire debris flow susceptibility



727

728 **Fig. 11** MRMS accumulated precipitation and peak discharge informed regional debris flow  
 729 susceptibility. (a) MRMS accumulated precipitation during January 27<sup>th</sup> 00:00 to 29<sup>th</sup> 23:00 over  
 730 the model domain (mm; shading). Names of burn scars are labeled in black. (b) Peak streamflow  
 731 ( $\text{m}^3 \text{s}^{-1}$ ; yellow-to-red shading) and (c) peak overland flow from 27<sup>th</sup> 00:00 to 28<sup>th</sup> 12:00 over the  
 732 model domain ( $\text{m}^3 \text{s}^{-1}$ ; yellow-to-red shading). (d)–(e) Stream-level postfire debris flow  
 733 susceptibility as Fig. 9b but for River and Camel burn scars. (f)–(g) Catchment-area normalized  
 734 debris flow susceptibility as Fig. 9e but for River and Camel burn scars. Wildfire perimeters of

735 2020 wildfire season are outlined in black in (a), in blue in (b), (c), (f), and (g), and in red in (d)  
736 and (e). The coastline of California is depicted in grey.

737  
738 In addition to investigating the operationalization of WRF-Hydro's natural hazard prediction  
739 capabilities, we note that with additional work our susceptibility-focused methodology could be  
740 advanced to the level of hazard assessment, in line with current USGS debris flow products. The  
741 USGS Emergency Assessment of Postfire Debris-flow Hazard predicts debris flow volume and  
742 likelihood. To advance from susceptibility to hazard assessment, our methodology would need to  
743 incorporate both debris flow volume estimates and occurrence likelihoods. In the following, we  
744 highlight research directions that could help advance our susceptibility-focused methodological  
745 framework. The first capability to develop would be a runoff-generated debris flow model that  
746 couples hydrologic and sediment erosion and transport processes to help characterize postfire  
747 debris flow volumes. Indeed, previous efforts have demonstrated the capacity to couple WRF-  
748 Hydro with sediment flux models (Yin et al., 2020; Shen et al., 2021). In addition to sediments,  
749 burn scar ash can comprise a substantial fraction of the total debris flow volume (e.g., Reneau et  
750 al., 2007). As such, efforts to constrain ash availability and entrainment in hydrologic flows could  
751 prove fortuitous in hazard assessment and prediction efforts. A second capability in need of  
752 development is the use of WRF-Hydro to identify debris flow triggering time and location by  
753 employing a domain-specific rainfall ID threshold trained with historic landslide inventory and  
754 triggering rainfall events (Tognacca et al., 2000; Gregoretti & Dalla Fontana, 2007, 2008) or a  
755 newly developed dimensionless discharge and Shields stress threshold (Tang et al., 2019a;  
756 McGuire & Youberg, 2020). While in this study we do not attempt to simulate debris flow  
757 dynamics such as triggering, we note that WRF-Hydro is capable of simulating overland flow and  
758 streamflow at higher spatiotemporal resolutions [on scales that are similar to other debris flow  
759 mechanistic studies such as Rengers et al. (2016), McGuire et al. (2016, 2017), and Tang et al.  
760 (2019a, 2019b)]. Therefore, WRF-Hydro's capability to simulate the triggering processes of  
761 runoff-generated debris flows is potentially only limited by the spatiotemporal resolution of  
762 precipitation forcing and computing resources.

763  
764 In addition to constraining postfire debris flow volumes and occurrence likelihoods, WRF-Hydro's  
765 application in debris flow studies could be advanced via concerted engagement with uncertainties  
766 that are both external (meteorological forcing data) and internal (physical parameters) to the model.  
767 Previous studies have demonstrated that precipitation is often the largest source of uncertainty in  
768 hydrologic predictive models (Hapuarachchi et al., 2011; Alfieri et al., 2012). Engagement with  
769 precipitation forcing uncertainties in past, near-term, and future contexts could provide  
770 probabilistic nuance to natural hazard investigations. For example, (a) debris flow hindcast studies  
771 could use a diversity of precipitation datasets to isolate precipitation-derived debris flow  
772 uncertainties in historic events, (b) operational forecast efforts could utilize ensemble-based  
773 weather forecast data to inform likelihood statements in debris flow hazard assessments, and (c)  
774 probabilistic projections of debris flow likelihood in future climates could assess and partition



775 uncertainties derived from emission pathway, model structure, or internal variability effects on  
776 meteorological forcings (Nikolopoulos et al., 2019; Hawkins & Sutton, 2009; Deser et al., 2020).  
777 Uncertainties internal to WRF-Hydro are also ripe for investigation. Probabilistic predictions  
778 crafted from an ensemble of perturbed model physics simulations have been used to predict  
779 rainfall-triggered shallow landslides (Raia et al., 2014; Canli et al., 2018; Zhang et al., 2018).  
780 Similar efforts using WRF-Hydro could target post-wildfire debris flows.

781  
782  
783 Lastly, the above discussion of potential WRF-Hydro applications and advancements speaks to the  
784 adaptability and customization of this open-source numerical model. An additional layer of WRF-  
785 Hydro's adaptability concerns its geographic focus. While we calibrate and use the model over a  
786 central California domain, the choice of geographic footprint is only limited by the availability of  
787 requisite initial and boundary conditions, environmental observations for calibration, and  
788 computational resources. For use in non-central California domains, we recommend calibration  
789 beginning with the default version of the model. Given the ecological and geological diversity of  
790 locations that experience wildfires and debris flows, it is likely that calibrations distinct from those  
791 reported here will be needed in different regions. For example, soil sealing effects, infiltration, and  
792 runoff in wetter and more vegetated locations, such as Oregon, USA, behave differently than those  
793 in central California (Palmer, 2022). As such, calibration of relevant model parameters (e.g.,  
794 saturated hydraulic conductivities) should be based on a physics-informed approach that accounts  
795 for local environmental conditions and hydrologic behaviors. Indeed, given the ability to simulate  
796 large heterogeneous geographic domains, it is likely that different regions within a given domain  
797 may require different calibration schemes. As WRF-Hydro is fully distributed, spatially  
798 heterogeneous calibrations are non-problematic. This spatial adaptability may prove particularly  
799 helpful in post-wildfire debris flow hazard assessments when considering multiple generations of  
800 wildfires and variable degrees of burn scar severity and recovery.

## 801 **7 Conclusion**

802 Here we augment WRF-Hydro to assess regional postfire debris flow susceptibility. Our  
803 methodology involves output of simulated overland flow data and alteration of the model's  
804 representation of burn scars. In this application we have balanced the computational cost of a  
805 regional domain with our choice of resolved spatial resolution for terrain routing and overland  
806 flow calculations (100 m). However, WRF-Hydro has previously been applied to smaller domains  
807 at higher terrain routing resolutions (~30 m). Future work could assess the use of the model to  
808 study burn scar hydrology at finer spatial scales, should the application warrant and should  
809 underlying data at sufficient resolution exist. Other potential applications of our augmented model  
810 framework include alpine areas and steep hillslopes with sparse vegetation where runoff-generated  
811 debris flows dominate over landslide-initiated ones (Davies et al., 1992; Coe et al., 2003, 2008).  
812 Furthermore, our burn scar parameter changes are performed to Noah-MP, which is the core land  
813 surface component of the NCEP Global Forecast System (GFS) and Climate Forecast System

814 (CFS), thus the findings presented herein, are likely to prove useful in the broader worlds of  
815 forecast meteorology and climate science. In addition, here WRF-Hydro is driven by historical  
816 precipitation and meteorological data, i.e., in hindcast mode. However, this modeling framework  
817 could also be employed to project hazards under future climatic conditions (e.g., Huang et al.,  
818 2020a), or given its relatively low computational expense, in operational forecast mode. Indeed,  
819 modern ensemble-based meteorological forecasting could provide high spatiotemporal forcing  
820 data with which disaster preparedness managers could probabilistically assess debris flow hazard  
821 potential, and issue advanced life and property saving warnings.

822  
823  
824

## 825 **Appendix A**

### 826 **Text A1. Multi-Radar/Multi-Sensor System (MRMS) radar-only precipitation estimate and** 827 **uncertainty**

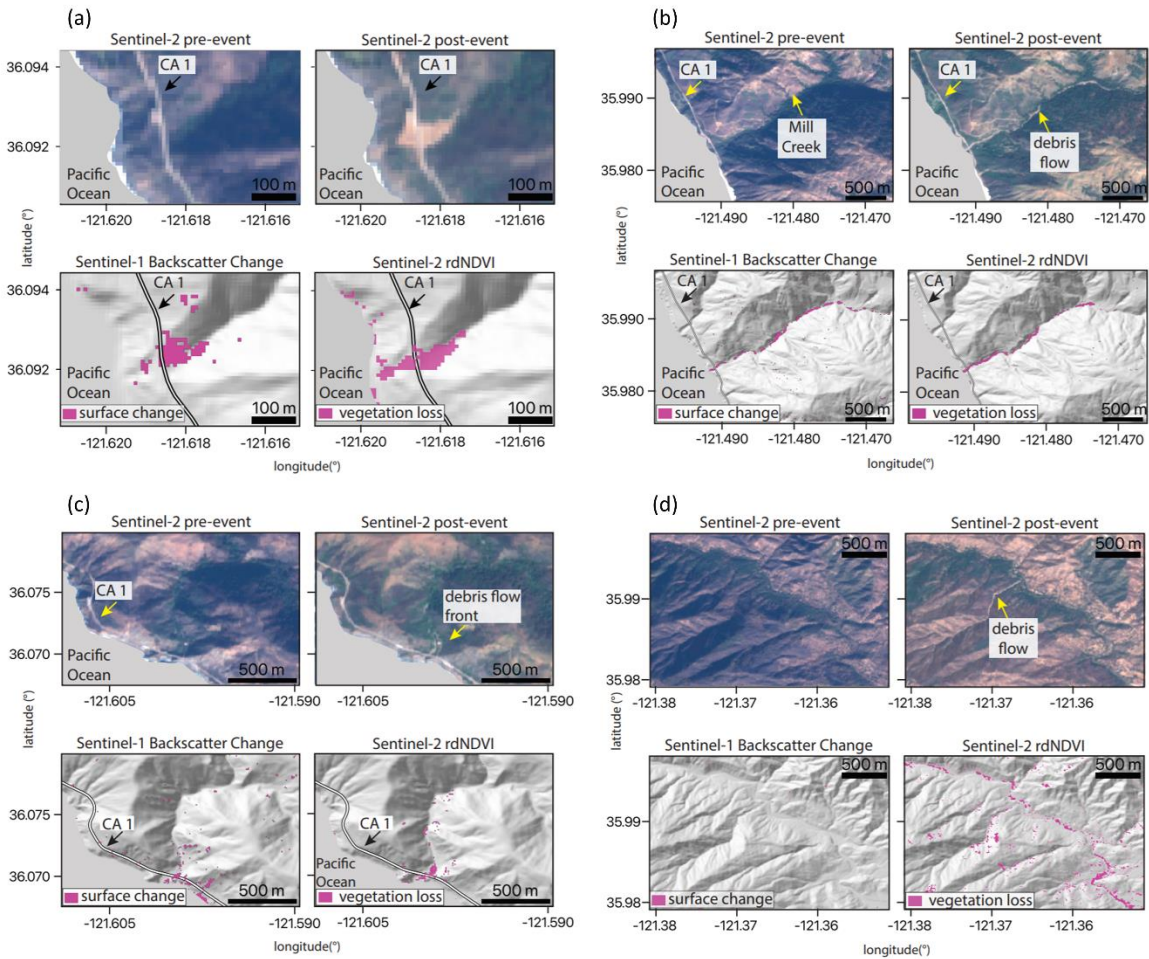
828 MRMS is a precipitation product that covers the contiguous United States (CONUS) on 1-km grids.  
829 It combines precipitation estimates from sensors and observational networks (Zhang et al.,  
830 2011, 2014, 2016), and is produced at the National Centers for Environmental Prediction (NCEP)  
831 and distributed to National Weather Service forecast offices and other agencies. Input datasets  
832 used to produce MRMS include the U.S. Weather Surveillance Radar-1988 Doppler (WSR-88D)  
833 network and Canadian radar network, Parameter-elevation Regressions on Independent Slopes  
834 Model (PRISM; Daly et al., 1994, 2017), Hydrometeorological Automated Data System (HADS)  
835 gauge data with quality control (Qi et al., 2016), and outputs from numerical weather prediction  
836 models. There are four different MRMS quantitative precipitation estimates (QPE) products  
837 incorporating different input data or combinations: radar only, gauge only, gauge-adjusted radar,  
838 and Mountain Mapper. One caveat of using MRMS is that weather radars are problematic in  
839 accurately capturing rainfall in high mountainous areas due to beam blocking by the orography  
840 (Anagnostou et al., 2010; Germann et al., 2007), and gauge-corrected and Mountain Mapper  
841 MRMS are superior and preferred. However, for our study period (i.e., January 1–31, 2021), the  
842 gauge-corrected and Mountain Mapper MRMS are not available (as of May 2022).

843

844 We acknowledge that precipitation data has uncertainties. Use of different precipitation products  
845 may produce different results. A study comparing different gridded precipitation datasets including  
846 satellite-based precipitation data, gauge dataset, and multi-sensor products revealed large  
847 uncertainties in precipitation intensity (Bytheway et al., 2020). However, comparing different  
848 precipitation datasets to characterize uncertainties is beyond the scope of this study. MRMS  
849 provides gridded precipitation at high temporal (hourly) and spatial (1-km) resolutions, making it  
850 a useful tool to demonstrate the utility of WRF-Hydro in post-wildfire debris flow susceptibility  
851 assessments.

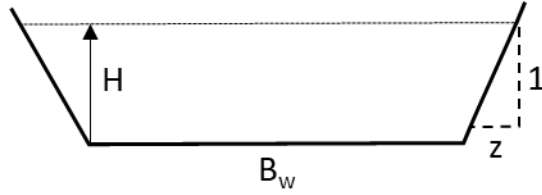


852 **Appendix B**



853  
 854  
 855  
 856  
 857  
 858  
 859  
 860  
 861  
 862  
 863  
 864

**Fig. B1** Optical- and SAR-based remote sensing data of four debris flows. Optical data from Sentinel-2 show pre- and post-debris flow imagery in real color. rdNDVI calculated from the Sentinel-2 data show a decrease in vegetation corresponding to debris flow locations. Sentinel-1 backscatter change shows the change in ground surface properties determined by calculating the log ratio of pre- and post-event SAR images. The pre-event, post-event satellite images, Sentinel-1 Backscatter, and Sentinel-2 rdNDVI change at (a) Rat Creek, (b) Mill Creek, (c) Big Creek, and (d) Nacimientos.



865

866

867

868

869

**Fig. B2** Schematic trapezoidal shape and related parameters of channels in WRF-Hydro.  $B_w$  is the channel bottom width (m),  $z$  is the channel side slope (m), and  $H$  is water elevation (m). The cross-sectional area of flow is calculated as  $(B_w + H z)H$ .

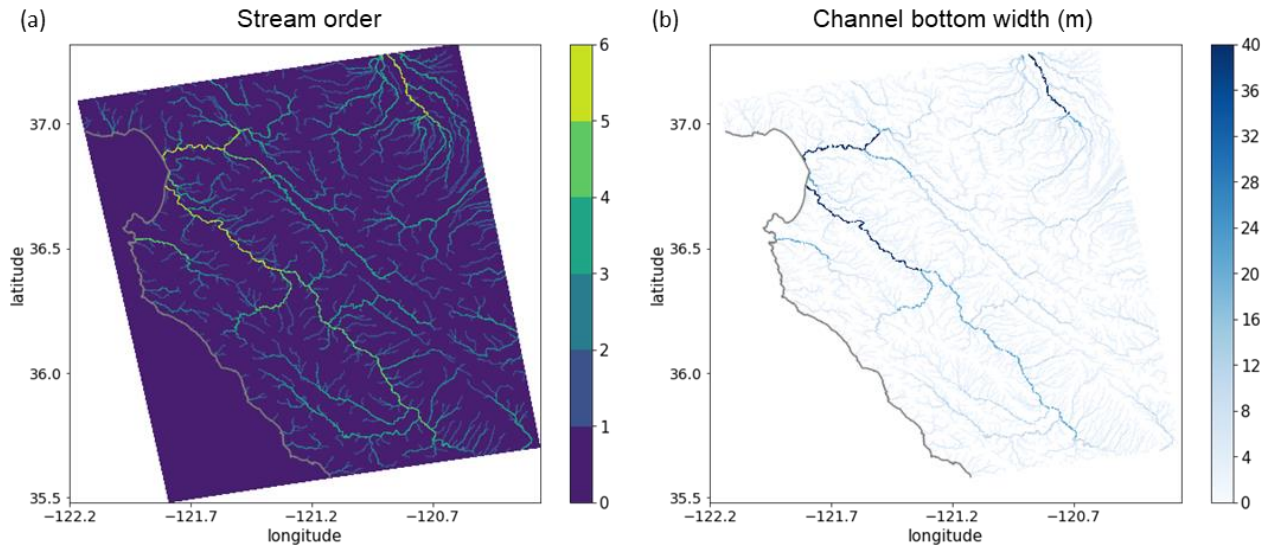
870 **Table B1** Parameters of trapezoidal channels in WRF-Hydro.

Stream order	Channel bottom width $B_w$ (m)	Channel side slope $z$ (m)	Manning's roughness coefficient $n$
1	1.5	3	0.33
2	3	1	0.21
3	5	0.5	0.09
4	10	0.18	0.06
5	20	0.05	0.04
6	40	0.05	0.03
7	60	0.05	0.02
8	70	0.05	0.02
9	80	0.05	0.01
10	100	0.05	0.01

871  
 872 **Table B1** Parameters of the trapezoidal channels in WRF-Hydro including channel bottom width  
 873  $B_w$  (m), channel side slope  $z$  (m), and Manning's roughness coefficient  $n$ .

874

875



876

877 **Fig. B3** (a) Stream order defined by the USGS 30-m DEM in our WRF-Hydro model domain  
 878 and (b) the channel bottom width (m) which is a function of stream order (Table B1).

879

880 *Table B2*

881 *MODIS IGBP 20-category land cover type and properties in Noah-MP LSM*

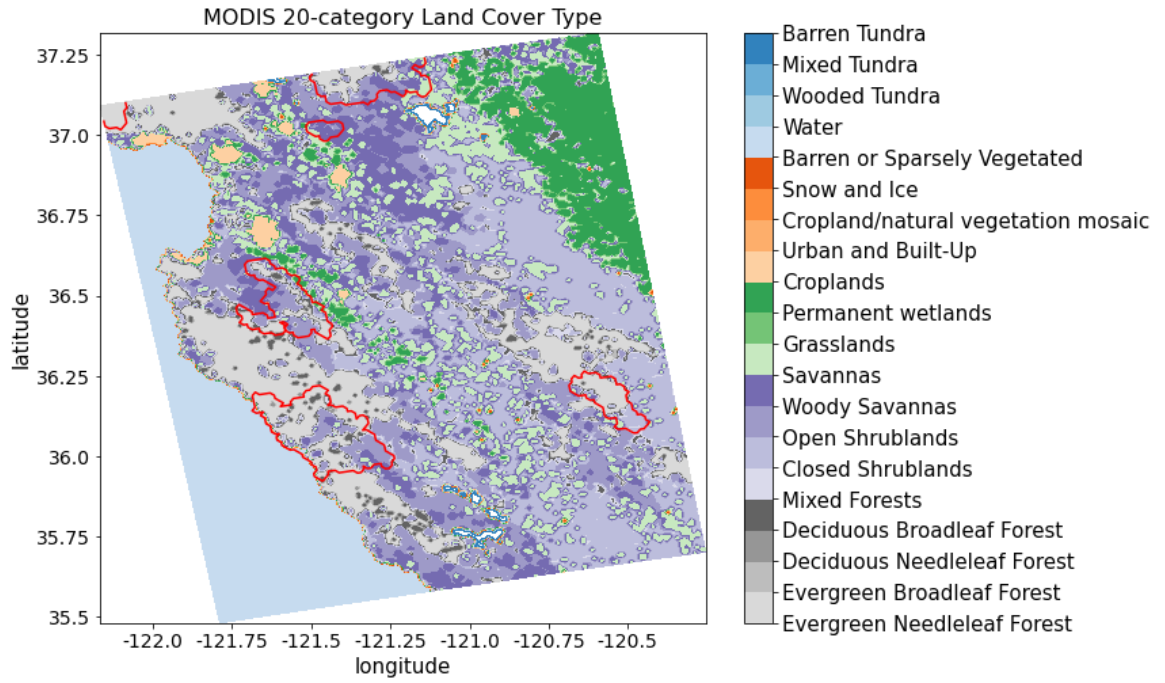
Land cover code	Land cover type	Canopy height (m)	Max carboxylation rate at 25°C ( $\mu\text{mol CO}_2/(\text{m}^2 \cdot \text{s})$ )	Overland flow roughness
1	Evergreen Needleleaf Forest	20	50	0.2
2	Evergreen Broadleaf Forest	20	60	0.2
3	Deciduous Needleleaf Forest	18	60	0.2
4	Deciduous Broadleaf Forest	16	60	0.2
5	Mixed Forests	16	55	0.2
6	Closed Shrublands	1.1	40	0.055
7	Open Shrublands	1.1	40	0.055
8	Woody Savannas	13	40	0.055
9	Savannas	10	40	0.055
10	Grasslands	1	40	0.055
11	Permanent wetlands	5	50	0.07
12	Croplands	2	80	0.035
13	Urban and Built-Up	15	0	0.025
14	Cropland/natural vegetation mosaic	1.5	60	0.035
15	Snow and Ice	0	0	0.01
16	Barren or Sparsely Vegetated	0	0	0.035
17	Water	0	0	0.005
18	Wooded Tundra	4	50	0.055
19	Mixed Tundra	2	50	0.055
20	Barren Tundra	0.5	50	0.055

882

883 **Table B2** MODIS IGBP 20-category land cover type and properties in Noah-MP LSM.

884

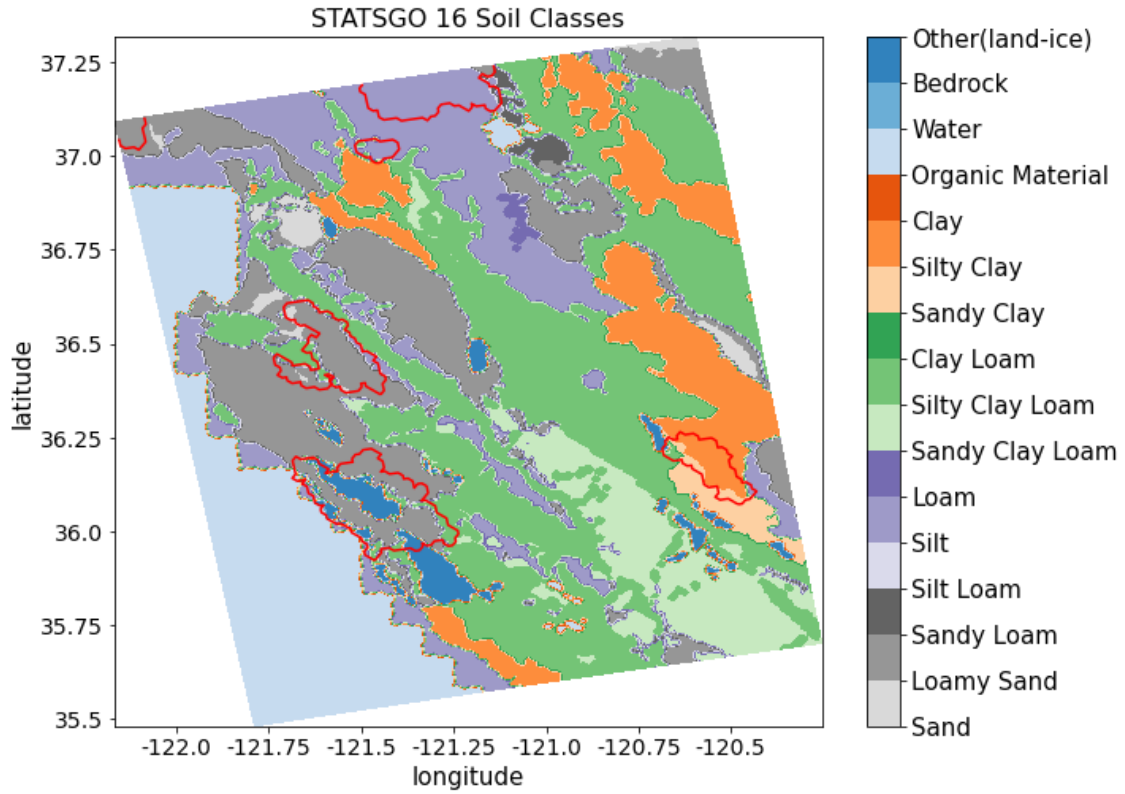
885



886 **Fig. B4** MODIS IGBP 20-category land cover type in the model domain. Red polylines are 2020  
 887 wildfire burn scar perimeters.

888

889



890 **Fig. B5** 1-km STATSGO data with 16 soil texture types. Red polylines are 2020 wildfire burn  
 891 scar perimeters.

892  
 893  
 894  
 895  
 896

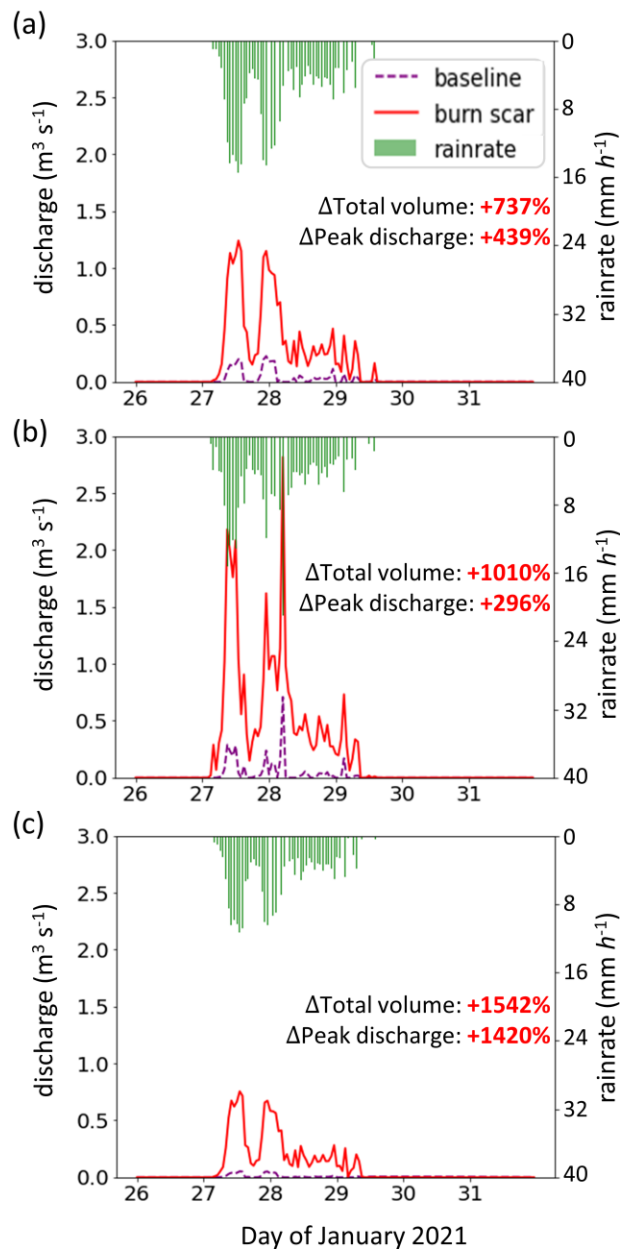
897 *Table B3*  
 898 *Default and calibrated soil parameters in WRF-Hydro*  
 899

Soil type	Default			After calibration		
	Grain size distribution index	Porosity	Saturated hydraulic conductivity (m s <sup>-1</sup> )	Grain size distribution index	Porosity	Saturated hydraulic conductivity (m s <sup>-1</sup> )
Sand	2.79	0.339	4.66E-5	2.51	0.315	1.5 x 10 <sup>-7</sup> m s <sup>-1</sup> for all the burn scars, and original values elsewhere.
Loamy sand	4.26	0.421	1.41E-5	3.83	0.392	
Sandy loam	4.74	0.434	5.23E-6	4.27	0.404	
Silt loam	5.33	0.476	2.81E-6	4.80	0.442	
Silt	3.86	0.484	2.18E-6	3.47	0.450	
Loam	5.25	0.439	3.38E-6	4.73	0.408	
Sandy clay loam	6.77	0.404	4.45E-6	6.09	0.376	
Silty clay loam	8.72	0.464	2.03E-6	7.85	0.432	
Clay loam	8.17	0.465	2.45E-6	7.35	0.432	
Sandy clay	10.73	0.406	7.22E-6	9.66	0.378	
Silty clay	10.39	0.468	1.34E-6	9.35	0.435	
Clay	11.55	0.468	9.74E-7	10.40	0.435	
Organic material	5.25	0.439	3.38E-6	4.73	0.408	
Water	0.00	1.00	0.00	0.00	1.00	
Bedrock	2.79	0.200	1.41E-4	2.51	0.186	
Other	4.26	0.421	1.41E-5	3.83	0.392	
Playa	11.55	0.468	9.74E-7	10.40	0.435	
Lava	2.79	0.200	1.41E-4	2.51	0.186	
White sand	2.79	0.339	4.66E-5	2.51	0.315	

900  
 901 **Table B3** Soil parameters in default and calibrated WRF-Hydro. Default soil parameters in WRF-  
 902 Hydro are adapted from the soil analysis by Cosby et al. (1984). Grain size distribution index and  
 903 soil porosity are altered from default values during the global soil moisture calibration. Saturated  
 904 hydraulic conductivity is altered from default values during the streamflow calibration.  
 905

906





907  
 908  
 909  
 910  
 911  
 912  
 913  
 914

**Fig. B6** WRF-Hydro simulated discharge time-series at four debris flow source areas. (a)–(c) MRMS precipitation (green bars) and simulated discharge time-series for January 26<sup>th</sup> 00:00 to 31<sup>st</sup> 23:00 at Mill Creek, Big Creek, and Nacimiento debris flow source areas (black circles in Fig. 7b–d) in baseline (purple dashed line) and burn scar simulation (red line).

915 *Table B4*

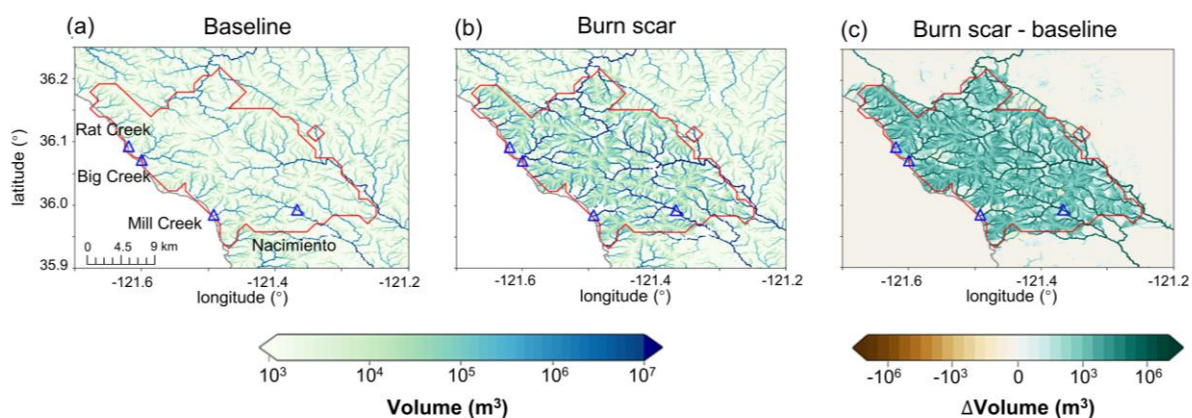
916 *The total runoff volume, peak discharge, and peak timing at debris-flow source areas*

Site name	Baseline simulation			Burn scar simulation		
	Total volume (m <sup>3</sup> )	Peak discharge (m <sup>3</sup> s <sup>-1</sup> )	Peak timing	Total volume (m <sup>3</sup> )	Peak discharge (m <sup>3</sup> s <sup>-1</sup> )	Peak timing
Mill Creek	10,023	0.23	27 <sup>th</sup> 23:00	83,853 (+737%)	1.24 (+439%)	27 <sup>th</sup> 13:00
Big Creek	11,611	0.71	28 <sup>th</sup> 05:00	128,879 (+1010%)	2.81 (+296%)	28 <sup>th</sup> 05:00
Nacimiento	3,031	0.05	27 <sup>th</sup> 13:00	49,792 (+1542%)	0.76 (+1420%)	27 <sup>th</sup> 13:00

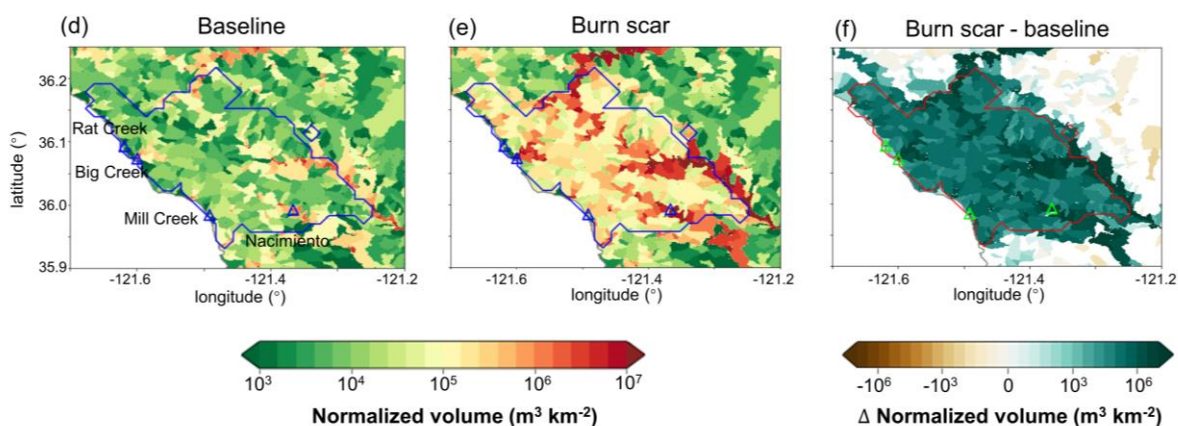
917  
 918 **Table B4** The total runoff volume, peak discharge, and peak timing in the baseline and burn scar  
 919 simulations from January 27<sup>th</sup> 00:00 to 31<sup>st</sup> 23:00 at source areas of Rat Creek, Mill Creek, Big  
 920 Creek, and Nacimiento debris flows (black circles in Fig. 7b–d). The percent change of the total  
 921 volume and peak discharge in the burn scar simulation relative to the baseline simulation are shown  
 922 in parentheses.

923  
 924  
 925  
 926  
 927  
 928  
 929  
 930  
 931  
 932  
 933  
 934  
 935  
 936  
 937  
 938  
 939  
 940  
 941

### Stream channel accumulated discharge volume



### Catchment-area normalized accumulated discharge volume



942  
 943 **Fig. B7** Accumulated discharge volume at individual stream level for the (a) baseline, (b) burn  
 944 scar, and (c) difference between burn scar and baseline simulations ( $m^3$ ). Total discharge volume  
 945 is accumulated from January 27th 00:00 to 28th 12:00. (d)–(f) Normalized discharge volume by  
 946 catchment area at catchment level ( $m^3 km^{-2}$ ; shading; Santi & Morandi, 2013). For each catchment,  
 947 the discharge volume is accumulated at the catchment outlet from January 27<sup>th</sup> 00:00 to 28<sup>th</sup> 12:00  
 948 divided by catchment area. Triangles stand for debris flow deposition locations and are annotated  
 949 in (a) and (d).

950

951

952

953

954

955 *Table B5*

956 *Statistics of catchment area-normalized discharge volume in baseline and burn scar simulations*

	<b>mean</b>	<b>std</b>	<b>5P</b>	<b>25P</b>	<b>50P</b>	<b>75P</b>	<b>95P</b>
<b>Baseline simulation</b> (m <sup>3</sup> km <sup>-2</sup> )	380k	± 1.6M	0.6k	3.7k	13k	120k	2.1M
<b>Burn scar simulation</b> (m <sup>3</sup> km <sup>-2</sup> )	5.5M	± 23.0M	1.5k	30.7k	135k	1.3M	29.1M
<b>Relative percent change</b>	1300%	1400%	148%	725%	924%	980%	1300%

957 **Table B5** Statistics, including the mean, standard deviation (std), 5P, 25P, 50P, 75P, and 95P, of  
958 the catchment-area normalized discharge volume for all the 404 basins within the Dolan burn scar  
959 in the baseline and burn scar simulation and their relative percent changes.

960

961

962

963

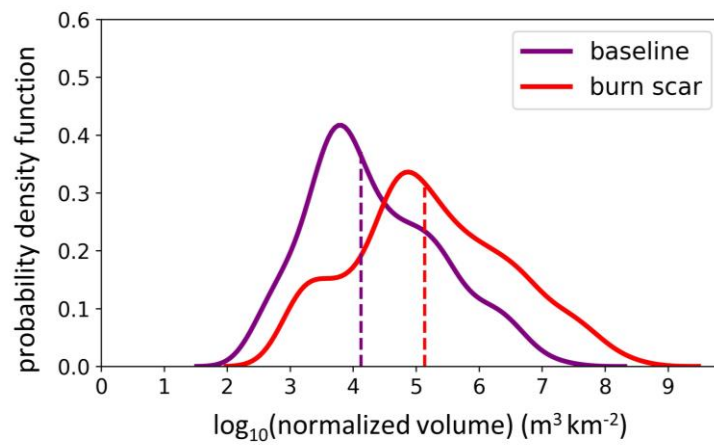
964

965

966

967

Distribution of catchment-area normalized volume



968

969 **Fig. B8** Distributions of accumulated discharge volumes at the outlet of the 404 catchments  
970 normalized by upstream catchment areas within Dolan burn scar in the baseline simulation (purple  
971 line) and in the burn scar simulation (red line). Dashed vertical lines indicate median values.

972

973

974

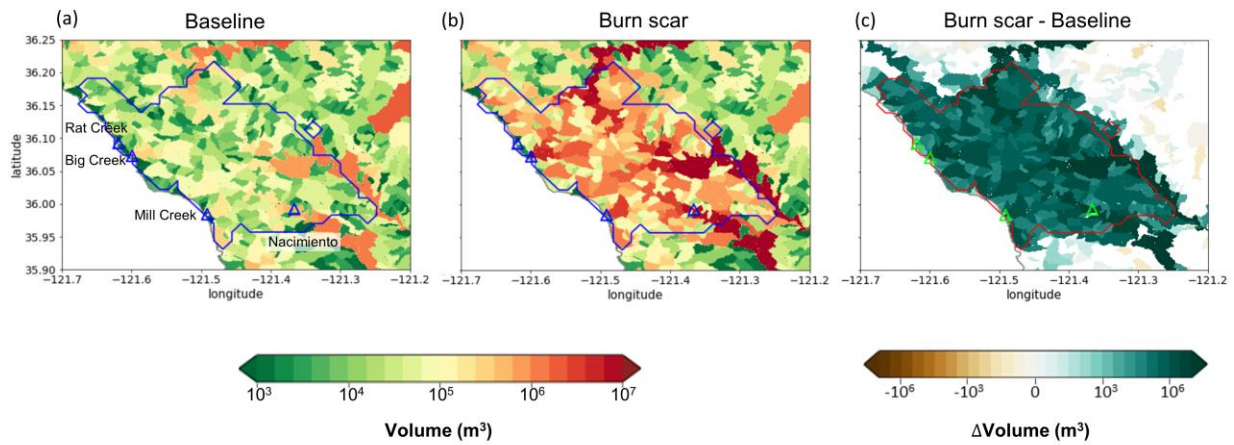
975

976

977

978

### Non-normalized catchment accumulated discharge volume



979

980

981 **Fig. B9** Non-normalized accumulated discharge volume at catchment level in the (a) baseline  
982 simulation, (b) burn scar simulation, and (c) the difference between the burn scar and baseline  
983 simulations ( $m^3$ ; shading). For each catchment, the discharge volume is accumulated at the  
984 catchment outlet from January 27<sup>th</sup> 00:00 to 28<sup>th</sup> 12:00. Triangles stand for debris flow deposition  
985 locations and are annotated in (a).

986

987

988

989

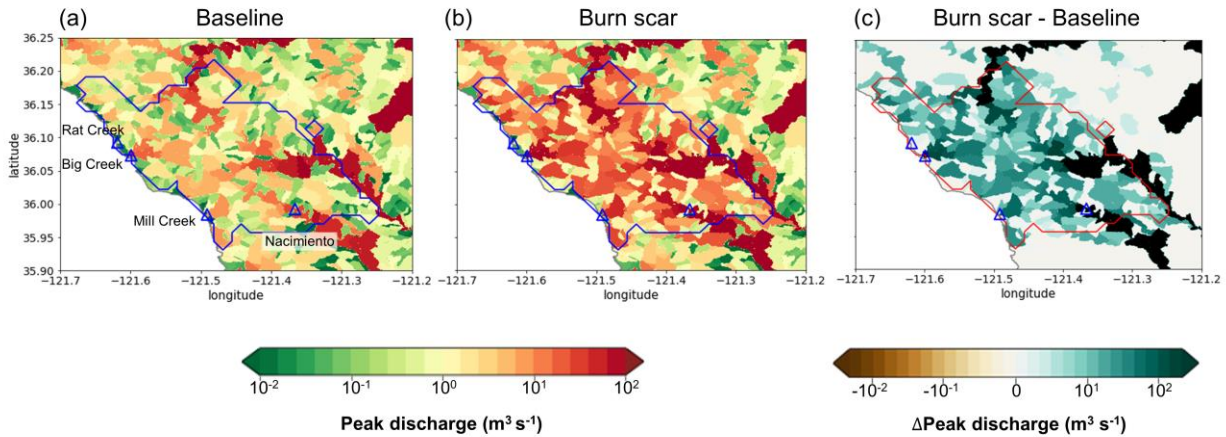
990

991

992

993

## Non-normalized catchment peak discharge



994

995 **Fig. B10** Non-normalized peak discharge at catchment level in the (a) baseline simulation, (b) burn  
996 scar simulation, and (c) the difference between the burn scar and baseline simulations ( $\text{m}^3 \text{s}^{-1}$ ;  
997 shading). For each catchment, the peak discharge is the maximum discharge rate at the catchment  
998 outlet from January 27<sup>th</sup> 00:00 to 28<sup>th</sup> 12:00. Triangles stand for debris flow deposition locations  
999 and are annotated in (a).

1000

1001

1002

1003

1004

### 1005 Data availability statement

1006 The NLDAS-2 reanalysis forcing data is publicly available at NASA GES DISC:  
1007 <https://disc.gsfc.nasa.gov/datasets?keywords=NLDAS>. A detailed description can be found at  
1008 <https://ldas.gsfc.nasa.gov/nldas/v2/forcing>. The MRMS radar-only precipitation estimate is  
1009 publicly available at: <https://mtarchive.geol.iastate.edu/>. A description can be found at  
1010 <https://www.nssl.noaa.gov/projects/mrms/>. The PSL in-situ soil moisture data is publicly available  
1011 at: <https://psl.noaa.gov/data/obs/datadisply/>. The USGS streamflow is publicly available at:  
1012 <https://waterdata.usgs.gov/nwis/>. The wildfire perimeter shapefiles are downloadable at:  
1013 <https://data-nifc.opendata.arcgis.com/search?collection=Dataset>. The remote sensing data used in  
1014 this manuscript were provided by the European Space Agency (ESA) Copernicus program and  
1015 accessed on Google Earth Engine (<https://code.earthengine.google.com>). All processed data  
1016 required to reproduce the results of this study are archived on Zenodo at  
1017 <http://doi.org/10.5281/zenodo.5544083>.



1018 **Code availability statement**

1019 The modified WRF-Hydro Fortran code and instructions to output the overland flow at terrain  
1020 routing grid can be downloaded at <https://github.com/NU-CCRG/Modified-WRF-Hydro>.

1021 HazMapper v1.0 is available at <https://hazmapper.org/>. The SAR backscatter change method code  
1022 is available at [https://github.com/MongHanHuang/GEE\\_SAR\\_landslide\\_detection](https://github.com/MongHanHuang/GEE_SAR_landslide_detection).

1023 **Author contribution**

1024 Conceptualization: CL, ALH, & DEH; Simulation and model analysis: CL; JW & WY model  
1025 methodological development. Remote sensing analysis: ALH; Field Observations: NJF; GIS  
1026 assistance: YX; Funding acquisition: GB & DH; CL wrote the original draft and all authors  
1027 reviewed and edited the manuscript.

1028 **Competing interests**

1029 The authors declare that they have no conflict of interest.

1030 **Acknowledgments**

1031 C.L., A.L.H., J.W., X.L., G.B., and D.E.H. acknowledge support from NSF PREEVENTS  
1032 #1848683. We acknowledge high-performance computing support from Cheyenne  
1033 (doi:10.5065/D6RX99HX) provided by NCAR's Computational and Information Systems  
1034 Laboratory, sponsored by the National Science Foundation. We thank P. Santi, an anonymous  
1035 reviewer, and the editor for formal reviews, and F. K. Rengers for informal comments.  
1036

1037

1038 **References**

- 1039 Alfieri L., Salamon P., Pappenberger F., Wetterhall F., Thielen J. (2012). Operational early warning systems for  
1040 water-related hazards in Europe *Environmental Science & Policy* 21:35-49  
1041 doi:<https://doi.org/10.1016/j.envsci.2012.01.008>
- 1042 Anderson, H. W., Hoover, M. D., & Reinhart, K. G. (1976). *Forests and water: effects of forest management on*  
1043 *floods, sedimentation, and water supply* (Vol. 18): Department of Agriculture, Forest Service, Pacific  
1044 Southwest Forest and Range Experiment Station, Berkeley, CA.
- 1045 Andersson, J. C. M., Arheimer, B., Traoré, F., Gustafsson, D., & Ali, A. (2017). Process refinements improve a  
1046 hydrological model concept applied to the Niger River basin. *Hydrological Processes*, 31(25), 4540-  
1047 4554. doi:<https://doi.org/10.1002/hyp.11376>
- 1048 Anagnostou MN, Kalogiros J, Anagnostou EN, Tarolli M, Papadopoulos A, Borga MJJoh (2010) Performance  
1049 evaluation of high-resolution rainfall estimation by X-band dual-polarization radar for flash flood  
1050 applications in mountainous basins 394:4-16



1051 Arattano, M., & Franzi, L. (2010). On the application of kinematic models to simulate the diffusive processes of  
1052 debris flows. *Nat. Hazards Earth Syst. Sci.*, 10(8), 1689-1695. doi:10.5194/nhess-10-1689-2010

1053 Arattano, M., & Savage, W.Z. (1994). Modelling debris flows as kinematic waves. *Bulletin of the International*  
1054 *Association of Engineering Geology* 49, 3–13. <https://doi.org/10.1007/BF02594995>

1055 Bart, R. (2016). A regional estimate of postfire streamflow change in California. *Water Resources Research*, 52,  
1056 n/a-n/a. doi:10.1002/2014WR016553

1057 Bart, R., & Hope, A. (2010). Streamflow response to fire in large catchments of a Mediterranean-climate region  
1058 using paired-catchment experiments. *Journal of Hydrology*, 388, 370-378.  
1059 doi:10.1016/j.jhydrol.2010.05.016

1060 Barth NA, Villarini G, Nayak MA, White K (2017) Mixed populations and annual flood frequency estimates in  
1061 the western United States: The role of atmospheric rivers *Water Resour Res* 53:257-269

1062 Brabb E.E. (1985) Innovative approaches to landslide hazard and risk mapping. In: *International Landslide*  
1063 *Symposium Proceedings*, Toronto, Canada. pp 17-22

1064 Bisson M., Favalli M., Fornaciai A., Mazzarini F., Isola I., Zanchetta G., & Pareschi M.T. (2005). A rapid method  
1065 to assess fire-related debris flow hazard in the Mediterranean region: An example from Sicily (southern  
1066 Italy) *International Journal of Applied Earth Observation and Geoinformation* 7:217-231  
1067 doi:<https://doi.org/10.1016/j.jag.2005.04.003>

1068 Bitew, M. M., & Gebremichael, M. (2011). Assessment of satellite rainfall products for streamflow simulation  
1069 in medium watersheds of the Ethiopian highlands. *Hydrol. Earth Syst. Sci.*, 15(4), 1147-1155.  
1070 doi:10.5194/hess-15-1147-2011

1071 Brown, E.K., Wang, J., & Feng, Y. (2020). U.S. wildfire potential: a historical view and future projection using  
1072 high-resolution climate data. *Environmental Research Letters*. 16, 034060

1073 Brunkal, H., & Santi, P. M. (2016). Exploration of design parameters for a dewatering structure for debris flow  
1074 mitigation. 208, 81-92.

1075 Bytheway, J. L., Hughes, M., Mahoney, K., & Cifelli, R. (2020). On the Uncertainty of High-Resolution Hourly  
1076 Quantitative Precipitation Estimates in California, *Journal of Hydrometeorology*, 21(5), 865-879.  
1077 Retrieved Oct 25, 2021, from [https://journals.ametsoc.org/view/journals/hydr/21/5/jhm-d-19-](https://journals.ametsoc.org/view/journals/hydr/21/5/jhm-d-19-0160.1.xml)  
1078 [0160.1.xml](https://journals.ametsoc.org/view/journals/hydr/21/5/jhm-d-19-0160.1.xml)

1079 Canfield, H. E., Goodrich, D. C., & Burns, I. S. (2005). Selection of parameters values to model post-fire runoff  
1080 and sediment transport at the watershed scale in southwestern forests. In *Managing watersheds for*  
1081 *human and natural impacts: engineering, ecological, and economic challenges* (pp. 1-12).

1082 Canli E., Mergili M., Thiebes B., & Glade T. (2018) Probabilistic landslide ensemble prediction systems: lessons  
1083 to be learned from hydrology *Nat Hazards Earth Syst Sci* 18:2183-2202 doi:10.5194/nhess-18-2183-  
1084 2018

1085 Cannon, S.H., Kirkham R.M., & Paise M., (2001). Wildfire-related debris-flow initiation processes, Storm King  
1086 Mountain, Colorado. *Geomorphology*, v.39, n. 3-4, 171-188

1087 Cannon, S. H., Gartner, J. E., Parrett, C., & Parise, M. (2003). Wildfire-related debris-flow generation through  
1088 episodic progressive sediment-bulking processes, western USA. *Debris-Flow Hazards Mitigation:*  
1089 *Mechanics, Prediction, and Assessment*. Millpress, Rotterdam, pp. 71-82.

1090 Cannon, S. H., Gartner, J., Wilson, R., Bowers, J., & Laber, J. (2008). Storm Rainfall Conditions for Floods and  
1091 Debris Flows from Recently Burned Basins in Southwestern Colorado and Southern California.  
1092 *Geomorphology*, 96, 250-269. Doi:10.1016/j.geomorph.2007.03.019

1093 Cannon, S. H., & DeGraff, J. (2009). The increasing wildfire and postfire debris flow threat in western USA,  
1094 and implications for consequences of climate change. In *Landslides–disaster risk reduction* (pp. 177-  
1095 190): Springer.

- 1096 Cannon, S. H., Gartner, J. E., Rupert, M. G., Michael, J. A., Rea, A. H., & Parrett, C. (2010). Predicting the  
 1097 probability and volume of postwildfire debris flows in the intermountain western United States. *GSA*  
 1098 *Bulletin*, 122(1-2), 127-144. Doi:10.1130/B26459.1
- 1099 Cannon, S. H., Boldt, E. M., Laber, J. L., Kean, J. W., & Staley, D. M. J. N. H. (2011). Rainfall intensity–  
 1100 duration thresholds for postfire debris flow emergency-response planning. 59(1), 209-236.
- 1101 Cavagnaro, D. et al. (2021) Variability in hydrologic response to rainfall across a burn scar: observations from  
 1102 the Dolan Fire, California. AGU abstract.  
 1103 <https://agu.confex.com/agu/fm21/meetingapp.cgi/Paper/921613>
- 1104 Cerdà, A. (1998). Changes in overland flow and infiltration after a rangeland fire in a Mediterranean scrubland.  
 1105 *Hydrological Processes*, 12(7), 1031-1042. Doi:[https://doi.org/10.1002/\(SICI\)1099-](https://doi.org/10.1002/(SICI)1099-1085(19980615)12:7<1031::AID-HYP636>3.0.CO;2-V)  
 1106 [1085\(19980615\)12:7<1031::AID-HYP636>3.0.CO;2-V](https://doi.org/10.1002/(SICI)1099-1085(19980615)12:7<1031::AID-HYP636>3.0.CO;2-V)
- 1107 Chen, F., & Dudhia, J. (2001). Coupling an Advanced Land Surface–Hydrology Model with the Penn State–  
 1108 NCAR MM5 Modeling System. Part I: Model Implementation and Sensitivity, *Monthly Weather*  
 1109 *Review*, 129(4), 569-585. Retrieved Oct 24, 2021, from  
 1110 [https://journals.ametsoc.org/view/journals/mwre/129/4/1520-](https://journals.ametsoc.org/view/journals/mwre/129/4/1520-0493_2001_129_0569_caalsh_2.0.co_2.xml)  
 1111 [0493\\_2001\\_129\\_0569\\_caalsh\\_2.0.co\\_2.xml](https://journals.ametsoc.org/view/journals/mwre/129/4/1520-0493_2001_129_0569_caalsh_2.0.co_2.xml)
- 1112 Chen, L., Berli, M., & Chief, K. (2013). Examining Modeling Approaches for the Rainfall-Runoff Process in  
 1113 Wildfire-Affected Watersheds: Using San Dimas Experimental Forest. *JAWRA Journal of the*  
 1114 *American Water Resources Association*, 49(4), 851-866. Doi:<https://doi.org/10.1111/jawr.12043>
- 1115 Claessens L., Schoorl, J.M., & Veldkamp, A. (2007) Modelling the location of shallow landslides and their  
 1116 effects on landscape dynamics in large watersheds: An application for Northern New Zealand  
 1117 *Geomorphology* 87:16-27 doi:<https://doi.org/10.1016/j.geomorph.2006.06.039>
- 1118 Crosta G. B., & Frattini P. (2003) Distributed modelling of shallow landslides triggered by intense rainfall. *Nat*  
 1119 *Hazards Earth Syst Sci* 3:81-93 doi:10.5194/nhess-3-81-2003
- 1120 Cui, Y., Cheng, D., & Chan, D. (2018). Investigation of post-fire debris flows in Montecito. *ISPRS International*  
 1121 *Journal of Geo-Information*, 8(1), 5.
- 1122 Coe, J., Godt, J., Parise, M., & Moscarriello, A. (2003). Estimating debris flow probability using fan stratigraphy,  
 1123 historic records, and drainage-basin morphology, Interstate 70 highway corridor, central Colorado, USA.  
 1124 Paper presented at the Debris flow Hazards Mitigation: Mechanics, Prediction, and Assessment, edited  
 1125 by: Rickenmann, D. and Cheng, Ch., Proceedings 3<sup>rd</sup> International DFHM Conference, Davos,  
 1126 Switzerland.
- 1127 Coe, J. A., Kinner, D. A., & Godt, J. W. J. G. (2008). Initiation conditions for debris flows generated by runoff  
 1128 at Chalk Cliffs, central Colorado. 96(3-4), 270-297.
- 1129 Collow ABM, Mersiovsky H, Bosilovich MG (2020) Large-Scale Influences on Atmospheric River–Induced  
 1130 Extreme Precipitation Events along the Coast of Washington State *J Hydrometeor* 21:2139-2156  
 1131 doi:10.1175/JHM-D-19-0272.1
- 1132 Cosby, B. J., Hornberger, G. M., Clapp, R. B., & Ginn, T. R. (1984). A Statistical Exploration of the  
 1133 Relationships of Soil Moisture Characteristics to the Physical Properties of Soils. *Water Resources*  
 1134 *Research*, 20(6), 682-690. Doi:<https://doi.org/10.1029/WR020i006p00682>
- 1135 Cydzik, K., & Hogue, T. S. (2009). Modeling postfire response and recovery using the hydrologic engineering  
 1136 center hydrologic modeling system (HEC-HMS) 1. *JAWRA Journal of the American Water Resources*  
 1137 *Association*, 45(3), 702-714.
- 1138 Dahal, R.K., Hasegawa, S., Nonomura, A., Yamanaka, M., Dhakal, S., Paudyal, P. (2008) Predictive modelling  
 1139 of rainfall-induced landslide hazard in the Lesser Himalaya of Nepal based on weights-of-evidence  
 1140 *Geomorphology* 102:496-510 doi:<https://doi.org/10.1016/j.geomorph.2008.05.041>

1141 Daly, C., R. P. Neilson, & D. L. Phillips. (1994). A statistical-topographic model for mapping climatological  
1142 precipitation over mountainous terrain. *J. Appl. Meteor.*, 33, 140–147. **Error! Hyperlink reference not valid.**

1143 Daly, C., M. E. Slater, J. A. Roberti, S. H. Laseter, & L. W. Swift Jr. (2017). High-resolution precipitation  
1144 mapping in a mountainous watershed; Ground truth for evaluating uncertainty in a national precipitation  
1145 dataset. *Int. J. Climatol.*, 37, 124–137, <https://doi.org/10.1002/joc.4986>.

1146 Davies, T., Phillips, C., Pearce, A., & Zhang, X. J. I. P. (1992). Debris flow behaviour—an integrated overview.  
1147 *209(21)*, 225.

1148 Dekker, L. W., & Ritsema, C. J. (1994). How water moves in a water repellent sandy soil: 1. Potential and actual  
1149 water repellency. *Water Resources Research*, 30(9), 2507-2517.  
1150 Doi:<https://doi.org/10.1029/94WR00749>

1151 Deser, C. et al. (2020) Insights from Earth system model initial-condition large ensembles and future prospects  
1152 *Nature Climate Change* 10:277-286 doi:10.1038/s41558-020-0731-2

1153 Di Cristo, C., Iervolino, M., Moramarco, T., & Vacca, A. (2021). Applicability of Diffusive model for mud-  
1154 flows: An unsteady analysis. *Journal of Hydrology*, 600, 126512.  
1155 Doi:<https://doi.org/10.1016/j.jhydrol.2021.126512>

1156 Doerr, S. H., & Thomas, A. (2000). The role of soil moisture in controlling water repellency: New evidence  
1157 from forest soils in Portugal. *Journal of Hydrology*, 231-232, 134-147. Doi:10.1016/S0022-  
1158 1694(00)00190-6

1159 Eldardiry H, Mahmood A, Chen X, Hossain F, Nijssen B, Lettenmaier DP (2019) Atmospheric River–Induced  
1160 Precipitation and Snowpack during the Western United States Cold Season *J Hydrometeor* 20:613–630  
1161 doi:10.1175/JHM-D-18-0228.1

1162 Flannigan, M., Cantin, A. S., De Groot, W. J., Wotton, M., Newbery, A., & Gowman, L. M. (2013). Global  
1163 wildland fire season severity in the 21st century. *Forest Ecology and Management*, 294, 54-61.

1164 Friedel, M.J. (2011a). A data-driven approach for modeling post-fire debris-flow volumes and their uncertainty  
1165 *Environmental Modelling & Software* 26:1583-1598 doi:<https://doi.org/10.1016/j.envsoft.2011.07.014>

1166 Friedel, M.J. (2011b) Modeling hydrologic and geomorphic hazards across post-fire landscapes using a self-  
1167 organizing map approach *Environmental Modelling & Software* 26:1660-1674  
1168 doi:<https://doi.org/10.1016/j.envsoft.2011.07.001>

1169 Gartner, J. E., Cannon, S. H., & Santi, P. M. (2014). Empirical models for predicting volumes of sediment  
1170 deposited by debris flows and sediment-laden floods in the transverse ranges of southern California.  
1171 *Engineering Geology*, 176, 45-56. doi:<https://doi.org/10.1016/j.enggeo.2014.04.008>

1172 George, D. L., & Iverson, R. M. (2014). A depth-averaged debris flow model that includes the effects of evolving  
1173 dilatancy. II. Numerical predictions and experimental tests. *Proceedings of the Royal Society A:*  
1174 *Mathematical, Physical and Engineering Sciences*, 470(2170), 20130820. doi:10.1098/rspa.2013.0820

1175 Germann U, Galli G, Boscacci M, Bolliger M (2007) Radar Precipitation Measurement in a Mountainous Region  
1176 *Q J Roy Meteorol Soc* 132:1669-1692 doi:10.1256/qj.05.190

1177 Gochis, D. J., & Chen, F. (2003). Hydrological Enhancements to the Community Noah Land Surface Model (No.  
1178 NCAR/TN-454+STR). University Corporation for Atmospheric Research. doi:10.5065/D60P0X00

1179 Goodrich, D., Burns, I., Unkrich, C., Semmens, D., Guertin, D., Hernandez, M., . . . Levick, L. (2012).  
1180 KINEROS2/AGWA: model use, calibration, and validation. *Transactions of the ASABE*, 55, 1561-  
1181 1574. doi:10.13031/2013.42264

1182 Goss, M., Swain, D. L., Abatzoglou, J. T., Sarhadi, A., Kolden, C. A., Williams, A. P., & Diffenbaugh, N. S.  
1183 (2020). Climate change is increasing the likelihood of extreme autumn wildfire conditions across  
1184 California. *Environmental Research Letters*, 15(9), 094016. doi:10.1088/1748-9326/ab83a7

1185 Gregoretti, C., & Dalla Fontana, G. (2007). Rainfall threshold for the initiation of debris flows by channel-bed  
1186 failure in the Dolomites. *Debris-Flow Hazards Mitigation: Mechanics, Prediction, and Assessment*, 11-  
1187 22.

1188 Gregoretti, C., & Dalla Fontana, G. (2008). The triggering of debris flow due to channel-bed failure in some  
1189 alpine headwater basins of the Dolomites: analyses of critical runoff. *Hydrological Processes*, 22(13),  
1190 2248-2263. doi:<https://doi.org/10.1002/hyp.6821>

1191 Gupta, H. V., Kling, H., Yilmaz, K. K., & Martinez, G. F. (2009). Decomposition of the mean squared error and  
1192 NSE performance criteria: Implications for improving hydrological modelling. *Journal of Hydrology*,  
1193 377(1), 80-91. doi:<https://doi.org/10.1016/j.jhydrol.2009.08.003>

1194 Guzzetti, F., Reichenbach, P., Cardinali, M., Galli, M., & Ardizzone, F. J. G. (2005) Probabilistic landslide  
1195 hazard assessment at the basin scale 72:272-299

1196 Handwerger AL, Huang MH, Jones SY, Amatya P, Kerner HR, Kirschbaum DB (2022) Generating landslide  
1197 density heatmaps for rapid detection using open-access satellite radar data in Google Earth Engine Nat  
1198 Hazards Earth Syst Sci 22:753-773 doi:10.5194/nhess-22-753-2022

1199 Hapuarachchi, H.A.P., Wang, Q.J., & Pagano, T.C. (2011) A review of advances in flash flood forecasting.  
1200 *Hydrological processes*. 25:2771-2784 doi:<https://doi.org/10.1002/hyp.8040>

1201 Hawkins, E., Sutton, R. (2009) The Potential to Narrow Uncertainty in Regional Climate Predictions *Bull Amer*  
1202 *Meteor Soc* 90:1095-1108 doi:10.1175/2009BAMS2607.1

1203 Hecht, C. W., & Cordeira, J. M. (2017). Characterizing the influence of atmospheric river orientation and  
1204 intensity on precipitation distributions over North Coastal California. *Geophysical Research Letters*,  
1205 44(17), 9048-9058.

1206 Huang X., Stevenson, S., Hall, A.D. (2020a) Future warming and intensification of precipitation extremes: A  
1207 “double whammy” leading to increasing flood risk in California. *Geophysical Research Letters*,  
1208 47:e2020GL088679

1209 Huang X., Swain D.L., Hall A.D. (2020b) Future precipitation increase from very high resolution ensemble  
1210 downscaling of extreme atmospheric river storms in California 6:eaba1323  
1211 doi:10.1126/sciadv.aba1323 %J Science AdvancesIce, G. G., Neary, D. G., & Adams, P. W. (2004).  
1212 Effects of Wildfire on Soils and Watershed Processes. *Journal of Forestry*, 102(6), 16-20.  
1213 doi:10.1093/jof/102.6.16

1214 Iverson, R. M., & George, D. L. (2014). A depth-averaged debris flow model that includes the effects of evolving  
1215 dilatancy. I. Physical basis. *Proceedings of the Royal Society A: Mathematical, Physical and*  
1216 *Engineering Sciences*, 470(2170), 20130819. doi:10.1098/rspa.2013.0819

1217 Jolly, W. M., Cochrane, M. A., Freeborn, P. H., Holden, Z. A., Brown, T. J., Williamson, G. J., & Bowman, D.  
1218 M. J. S. (2015). Climate-induced variations in global wildfire danger from 1979 to 2013. *Nature*  
1219 *Communications*, 6(1), 7537. doi:10.1038/ncomms8537

1220 Julien, P. Y., Saghafian, B., & Ogden, F. L. (1995). RASTER-BASED HYDROLOGIC MODELING OF  
1221 SPATIALLY-VARIED SURFACE RUNOFF1. *JAWRA Journal of the American Water Resources*  
1222 *Association*, 31(3), 523-536. doi:<https://doi.org/10.1111/j.1752-1688.1995.tb04039.x>

1223 Kean, J. W., Staley, D. M., & Cannon, S. H. (2011). In situ measurements of postfire debris flows in southern  
1224 California: Comparisons of the timing and magnitude of 24 debris flow events with rainfall and soil  
1225 moisture conditions. *Journal of Geophysical Research F: Earth Surface*, 116(4).  
1226 doi:10.1029/2011JF002005

1227 Kean, J. W., McCoy, S. W., Tucker, G. E., Staley, D. M., & Coe, J. A. (2013). Runoff-generated debris flows:  
1228 Observations and modeling of surge initiation, magnitude, and frequency. *Journal of Geophysical*  
1229 *Research: Earth Surface*, 118(4), 2190-2207. doi:<https://doi.org/10.1002/jgrf.20148>

1230 Kean, J. W., & Staley, D. M. (2021). Forecasting the Frequency and Magnitude of Postfire Debris Flows Across  
1231 Southern California. *Earth's Future*, 9(3), e2020EF001735. doi:<https://doi.org/10.1029/2020EF001735>

1232 Kinoshita, A. M., & Hogue, T. S. (2015). Increased dry season water yield in burned watersheds in Southern  
1233 California. *Environmental Research Letters*, 10(1), 014003. doi:10.1088/1748-9326/10/1/014003

1234 Kling, H., Fuchs, M., & Paulin, M. (2012). Runoff conditions in the upper Danube basin under an ensemble of  
1235 climate change scenarios. *Journal of Hydrology*, 424-425, 264-277.  
1236 doi:<https://doi.org/10.1016/j.jhydrol.2012.01.011>

1237 Larsen, I., MacDonald, L., Brown, E., Rough, D., Welsh, M., Pietraszek, J., . . . Schaffrath, K. (2009). Causes  
1238 of Postfire Runoff and Erosion: Water Repellency, Cover, or Soil Sealing? *Soil Science Society of  
1239 America Journal - SSSAJ*, 73. doi:10.2136/sssaj2007.0432

1240 Lahmers, T. M., Gupta, H., Castro, C. L., Gochis, D. J., Yates, D., Dugger, A., . . . Hazenberg, P. J. J. o. H.  
1241 (2019). Enhancing the structure of the WRF-Hydro hydrologic model for semiarid environments. 20(4),  
1242 691-714.

1243 Lahmers, T. M., Castro, C. L., & Hazenberg, P. (2020). Effects of Lateral Flow on the Convective Environment  
1244 in a Coupled Hydrometeorological Modeling System in a Semiarid Environment, *Journal of  
1245 Hydrometeorology*, 21(4), 615-642. Retrieved Sep 29, 2021, from  
1246 <https://journals.ametsoc.org/view/journals/hydr/21/4/jhm-d-19-0100.1.xml>

1247 Leopold, L. B., M. G. Wolman, and J.P. Miller, *Fluvial Processes in Geomorphology*, W. H. Freeman, New  
1248 York, 1964

1249 MacDonald, L. H., & Huffman, E. L. (2004). Postfire soil water repellency: Persistence and soil moisture  
1250 thresholds. *Soil Science Society of America Journal*, 68, 1729-1734.

1251 Martin, D., & Moody, J. (2001). Comparison of Soil Infiltration Rates in Burned and Unburned Mountainous  
1252 Watersheds. *Hydrological Processes*, 15, 2893-2903. doi:10.1002/hyp.380

1253 McCormick, B. C., Eshleman, K. N., Griffith, J. L., & Townsend, P. A. (2009). Detection of flooding responses  
1254 at the river basin scale enhanced by land use change, *Water Resour. Res.*, 45, W08401,  
1255 doi:10.1029/2008WR007594.

1256 McGuire, L. A., Kean, J. W., Staley, D. M., Rengers, F. K., & Wasklewicz, T. A. (2016). Constraining the  
1257 relative importance of raindrop- and flow-driven sediment transport mechanisms in postwildfire  
1258 environments and implications for recovery time scales, *J. Geophys. Res. Earth Surf.*, 121, 2211– 2237,  
1259 doi:10.1002/2016JF003867

1260 McGuire, L. A., Rengers, F. K., Kean, J. W., & Staley, D. M. (2017). Debris flow initiation by runoff in a  
1261 recently burned basin: Is grain-by-grain sediment bulking or en masse failure to blame? *Geophysical  
1262 Research Letters*, 44(14), 7310-7319. doi:<https://doi.org/10.1002/2017GL074243>

1263 McGuire, L. A., & Youberg, A. M. (2020). What drives spatial variability in rainfall intensity-duration thresholds  
1264 for post-wildfire debris flows? Insights from the 2018 Buzzard Fire, NM, USA. *Landslides*, 17(10),  
1265 2385-2399. doi:10.1007/s10346-020-01470-y

1266 McMichael, C. E., & Hope, A. S. (2007). Predicting streamflow response to fire-induced landcover change:  
1267 implications of parameter uncertainty in the MIKE SHE model. *J Environ Manage*, 84(3), 245-256.  
1268 doi:10.1016/j.jenvman.2006.06.003

1269 Neiman, P. J., Ralph, F. M., Wick, G. A., Lundquist, J. D., & Dettinger, M. D. (2008). Meteorological  
1270 Characteristics and Overland Precipitation Impacts of Atmospheric Rivers Affecting the West Coast of  
1271 North America Based on Eight Years of SSM/I Satellite Observations, *Journal of Hydrometeorology*,  
1272 9(1), 22-47. Retrieved May 13, 2022, from  
1273 [https://journals.ametsoc.org/view/journals/hydr/9/1/2007jhm855\\_1](https://journals.ametsoc.org/view/journals/hydr/9/1/2007jhm855_1).

1274 Meixner, T., & Wohlgemuth, P. M. (2003). Climate variability, fire, vegetation recovery, and watershed  
1275 hydrology. In Proceedings of the First Interagency Conference on Research in the Watersheds, Benson,  
1276 Arizona (pp. 651-656).

1277 Meyer, G. A., & Wells, S. G. (1997). Fire-related sedimentation events on alluvial fans, Yellowstone National  
1278 Park, U.S.A. *Journal of Sedimentary Research*, 67(5), 776-791. doi:10.1306/D426863A-2B26-11D7-  
1279 8648000102C1865D

1280 Miller, D. A., & White, R. A. (1998). A Conterminous United States Multilayer Soil Characteristics Dataset for  
1281 Regional Climate and Hydrology Modeling, *Earth Interactions*, 2(2), 1-26. Retrieved Sep 27, 2021, from  
1282 [https://journals.ametsoc.org/view/journals/eint/2/2/1087-3562\\_1998\\_002\\_0001\\_acusms\\_2.3.co\\_2.xml](https://journals.ametsoc.org/view/journals/eint/2/2/1087-3562_1998_002_0001_acusms_2.3.co_2.xml)

1283 Mitsopoulos, I. D., & Mironidis, D. (2006). Assessment of post fire debris flow potential in a Mediterranean  
1284 type ecosystem. *WIT Transactions on Ecology and the Environment*, 90.

1285 Moody, J. A., Shakesby, R. A., Robichaud, P. R., Cannon, S. H., & Martin, D. A. (2013). Current research issues  
1286 related to post-wildfire runoff and erosion processes. *Earth-Science Reviews*, 122, 10-37.  
1287 doi:<https://doi.org/10.1016/j.earscirev.2013.03.004>

1288 Moriasi, D. N., Arnold, J. G., Van Liew, M. W., Bingner, R. L., Harmel, R. D., & Veith, T. L. (2007). Model  
1289 evaluation guidelines for systematic quantification of accuracy in watershed simulations. *Transactions*  
1290 *of the ASABE*, 50(3), 885-900.

1291 Nash, J. E., & Sutcliffe, J. V. (1970). River flow forecasting through conceptual models part I — A discussion  
1292 of principles. *Journal of Hydrology*, 10(3), 282-290. doi:[https://doi.org/10.1016/0022-1694\(70\)90255-](https://doi.org/10.1016/0022-1694(70)90255-6)  
1293 6

1294 Neary, D. G., Gottfried, G. J., & Ffolliott, P. F. (2003). Post-wildfire watershed flood responses. In Proceedings  
1295 of the 2nd International Fire Ecology Conference, Orlando, Florida (pp. 16-20).

1296 Nikolopoulos, E.I., Destro, E., Bhuiyan, M.A.E, Borga, M., & Anagnostou, E.N. (2018). Evaluation of predictive  
1297 models for postfire debris flow occurrence in the western United States *Nat Hazards Earth Syst Sci*  
1298 18:2331-2343 doi:10.5194/nhess-18-2331-2018

1299 Nikolopoulos, E.I., Schwartz, C., Zhang, X., & Anagnostou, E.N. (2019) Rainfall estimation uncertainty and  
1300 early warning procedures for post-fire debris flows. In: *Geophysical Research Abstracts*.

1301 Niu, G-Y et al. (2011) The community Noah land surface model with multiparameterization options (Noah-MP):  
1302 1. Model description and evaluation with local-scale measurements *J Geophys Res Atm* 116  
1303 doi:<https://doi.org/10.1029/2010JD015139>

1304 Nyman, P., Smith, H.G., Sherwin, C.B., Langhans, C., Lane, P.N. J., & Sheridan, G.J. (2015). Predicting  
1305 sediment delivery from debris flows after wildfire. *Geomorphology*, 250, 173-186.  
1306 doi:<https://doi.org/10.1016/j.geomorph.2015.08.023>

1307 Oakley N.S., Lancaster J.T., Kaplan M.L., Ralph F.M. (2017) Synoptic conditions associated with cool season  
1308 post-fire debris flows in the Transverse Ranges of southern California *Nat Hazards* 88:327-354  
1309 doi:10.1007/s11069-017-2867-6

1310 Oakley N.S., Cannon F., Munroe R., Lancaster J.T., Gomberg D., Ralph F.M. (2018) Brief Communication:  
1311 Meteorological and climatological conditions associated with the 9 January 2018 post-fire debris flows  
1312 in Montecito and Carpinteria, California, USA *Nat Hazards Earth Syst Sci* 18:3037-3043  
1313 doi:10.5194/nhess-18-3037-2018

1314 Oakley, N.S. (2021). A warming climate adds complexity to postfire hydrologic hazard planning. *Earth's Future*,  
1315 9, e2021EF002149. <https://doi.org/10.1029/2021EF002149>

1316 Ogden, F.L. (1997). CASC2D reference manual. Department of Civil & Environmental Engineering, University  
1317 of Connecticut, Storrs.

1318 Palmer, J. (2022). The devastating mudslides that follow forest fires. *Nature*.  
1319 <https://www.nature.com/articles/d41586-022-00028-3>.

1320 Parise, M., & Cannon, S.H. (2008) The effects of wildfires on erosion and debris-flow generation in  
1321 Mediterranean climatic areas: a first database. Proceedings of 1<sup>st</sup> World Landslide Forum. Tokyo, Japan,  
1322 pp 465–468

1323 Parise, M., & Cannon, S.H. (2009). A database on post-fire erosion rates and debris flows in Mediterranean-  
1324 Basin watersheds. EGU General Assembly, Abstracts, p. 1530.

1325 Parise, M., & Cannon, S.H. (2012) Wildfire impacts on the processes that generate debris flows in burned  
1326 watersheds *Nat Hazards* 61:217-227 doi:10.1007/s11069-011-9769-9

1327 Park, D.W., Lee, S.R., Vasu, N.N., Kang, S.H., Park, J.Y. (2016) Coupled model for simulation of landslides  
1328 and debris flows at local scale *Nat Hazards* 81:1653-1682 doi:10.1007/s11069-016-2150-2

1329 Polade, S.D., Gershunov, A., Cayan, D.R, Dettinger, M.D., & Pierce, D.W. (2017) Precipitation in a warming  
1330 world: Assessing projected hydro-climate changes in California and other Mediterranean climate  
1331 regions *Scientific Reports* 7:10783 doi:10.1038/s41598-017-11285-y

1332 Qi, Y., Martinaitis, S., Zhang, J., & Cocks, S. (2016). A real-time automated quality control of hourly rain gauge  
1333 data based on multiple sensors in MRMS system. *J. Hydrometeor.*, 17, 1675–1691,  
1334 <https://doi.org/10.1175/JHM-D-15-0188.1>.

1335 Raia, S., Alvioli, M., Rossi, M., Baum, R. L., Godt, J.W., & Guzzetti, F. (2014) Improving predictive power of  
1336 physically based rainfall-induced shallow landslide models: a probabilistic approach *Geosci Model Dev*  
1337 7:495-514 doi:10.5194/gmd-7-495-2014

1338 Ralph, F. M., Neiman, P. J., & Wick, G. A. (2004) Satellite and CALJET aircraft observations of atmospheric  
1339 rivers over the eastern North Pacific Ocean during the winter of 1997/98. *Mon. Wea. Rev.*, 132, 1721–  
1340 1745, [https://doi.org/10.1175/1520-0493\(2004\)132<1721:SACAOO>2.0.CO;2](https://doi.org/10.1175/1520-0493(2004)132<1721:SACAOO>2.0.CO;2).

1341 Regmi, N.R., Giardino, J.R., Vitek, J.D. (2010) Modeling susceptibility to landslides using the weight of  
1342 evidence approach: Western Colorado, USA *Geomorphology* 115:172-187  
1343 doi:<https://doi.org/10.1016/j.geomorph.2009.10.002>

1344 Reichenbach, P., Rossi, M., Malamud, B.D., Mihir, M., & Guzzetti, F. (2018) A review of statistically-based  
1345 landslide susceptibility models *Earth-Science Reviews* 180:60-91  
1346 doi:<https://doi.org/10.1016/j.earscirev.2018.03.001>

1347 Rengers, F.K., McGuire, L.A., Kean, J.W., Staley, D.M., & Hobley, D.E.J. (2016). Model simulations of flood  
1348 and debris flow timing in steep catchments after wildfire. *Water Resources Research*, 52(8), 6041-6061.  
1349 doi:<https://doi.org/10.1002/2015WR018176>

1350 Reneau, S.L., Katzman, D., Kuyumjian, G.A., Lavine, A., & Malmon, D.V. (2007). Sediment delivery after a  
1351 wildfire. *Geology*, 35(2), 151-154. doi:10.1130/G23288A.1

1352 Reynolds, C., (2021). Highway 1 washout near Big Sur expected to be fixed by summer, *Los Angeles Times*.  
1353 [https://www.latimes.com/travel/story/2021-02-25/highway-1-to-big-sur-will-reopen-by-summer-](https://www.latimes.com/travel/story/2021-02-25/highway-1-to-big-sur-will-reopen-by-summer-caltrans-says)  
1354 [caltrans-says](https://www.latimes.com/travel/story/2021-02-25/highway-1-to-big-sur-will-reopen-by-summer-caltrans-says)

1355 Robichaud, P., Beyers, J., & Neary, D. (2000). Evaluating the effectiveness of postfire rehabilitation treatments.

1356 Rosso, R., Rulli, M.C., Bocchiola, D. (2007) Transient catchment hydrology after wildfires in a Mediterranean  
1357 basin: runoff, sediment and woody debris *Hydrol Earth Syst Sci* 11:125-140 doi:10.5194/hess-11-125-  
1358 2007

1359 Rulli, M.C., & Rosso, R. (2007). Hydrologic response of upland catchments to wildfires. *Advances in Water*  
1360 *Resources*, 30(10), 2072-2086. doi:<https://doi.org/10.1016/j.advwatres.2006.10.012>

1361 Santi, P.M., deWolfe, V.G., Higgins, J.D., Cannon, S.H., & Gartner, J.E. (2008). Sources of debris flow material  
1362 in burned areas. *Geomorphology*, 96(3-4), 310-321. doi:10.1016/j.geomorph.2007.02.022

1363 Santi, P.M., & Morandi, L. (2013). Comparison of debris flow volumes from burned and unburned areas.  
1364 *Landslides*, 10(6), 757-769.



1365 Schaeffli, B., & Gupta, H. V. (2007). Do Nash values have value? *Hydrological Processes*, 21(15), 2075-2080.  
1366 <https://doi.org/10.1002/hyp.6825>

1367 Scheip, C.M., & Wegmann, K.W. (2021). HazMapper: A global open-source natural hazard mapping application  
1368 in Google Earth Engine. *Natural Hazards and Earth System Sciences*, 21(5), 1495-1511.

1369 Schönfelder, L. H., Bakken, T. H., Alfredsen, K., & Adera, A. G. (2017). Application of HYPE in Norway.  
1370 SINTEF Energi. Rapport.

1371 Scott, D. F., & Van Wyk, D. B. (1990). The effects of wildfire on soil wettability and hydrological behaviour of  
1372 an afforested catchment. 121, 239. doi:10.1016/0022-1694(90)90234-o

1373 Scott, D. F. (1993). The hydrological effects of fire in South African mountain catchments. *Journal of hydrology*,  
1374 150(2-4), 409-432.

1375 Shakesby, R. A., & Doerr, S. H. (2006). Wildfire as a hydrological and geomorphological agent. *Earth-Science*  
1376 *Reviews*, 74(3), 269-307. doi:<https://doi.org/10.1016/j.earscirev.2005.10.006>

1377 Shen H., Lynch, B., Poulsen, C.J., & Yanites, B.J. (2021) A modeling framework (WRF-Landlab) for simulating  
1378 orogen-scale climate-erosion coupling *Computers & Geosciences* 146:104625  
1379 doi:<https://doi.org/10.1016/j.cageo.2020.104625>

1380 Sidman, G., Guertin, D., Goodrich, D., Unkrich, C., & Burns, I. (2016). Risk assessment of post-wildfire  
1381 hydrological response in semiarid basins: the effects of varying rainfall representations in the  
1382 KINEROS2/AGWA model. *International Journal of Wildland Fire*, 25, 268-278. doi:10.1071/WF14071

1383 Staley, D. M., Negri, J. A., Kean, J. W., Laber, J. L., Tillery, A. C., & Youberg, A. M. (2016). Updated logistic  
1384 regression equations for the calculation of postfire debris flow likelihood in the western United States  
1385 (2016-1106). Retrieved from Reston, VA: <http://pubs.er.usgs.gov/publication/ofr20161106>

1386 Staley, D.M., Negri, J.A., Kean, J.W., Laber, J.L., Tillery, A.C., & Youberg, A. M. (2017) Prediction of spatially  
1387 explicit rainfall intensity–duration thresholds for post-fire debris-flow generation in the western United  
1388 States *Geomorphology* 278:149-162 doi:<https://doi.org/10.1016/j.geomorph.2016.10.019>

1389 Stoof, C.R., Vervoort, R.W., Iwema, J., van den Elsen, E., Ferreira, A.J.D., & Ritsema, C.J. (2012). Hydrological  
1390 response of a small catchment burned by experimental fire. *Hydrol. Earth Syst. Sci.*, 16(2), 267-285.  
1391 doi:10.5194/hess-16-267-2012

1392 Swain, D.L., Langenbrunner, B., Neelin, J.D., & Hall, A. (2018) Increasing precipitation volatility in twenty-  
1393 first-century California. *Nature Climate Change*. 8:427-433 doi:10.1038/s41558-018-0140-y

1394 Swain, D.L. (2021). A Shorter, Sharper Rainy Season Amplifies California Wildfire Risk. *Geophysical Research*  
1395 *Letters*, 48(5), e2021GL092843. doi:<https://doi.org/10.1029/2021GL092843>

1396 Tang, H., McGuire, L. A., Rengers, F. K., Kean, J. W., Staley, D. M., & Smith, J. B. (2019a). Developing and  
1397 testing physically based triggering thresholds for runoff-generated debris flows. *Geophysical Research*  
1398 *Letters*, 46, 8830– 8839. <https://doi.org/10.1029/2019GL083623>

1399 Tang, H., McGuire, L. A., Rengers, F. K., Kean, J. W., Staley, D. M., & Smith, J. B. (2019b). Evolution of  
1400 debris-flow initiation mechanisms and sediment sources during a sequence of postwildfire rainstorms.  
1401 *Journal of Geophysical Research: Earth Surface*, 124, 1572– 1595.  
1402 <https://doi.org/10.1029/2018JF004837>

1403 Tognacca, C., Bezzola, G.R., & Minor, H.E. (2000). Threshold criterion for debris-flow initiation due to channel-  
1404 bed failure. *Debris-flow hazards mitigation: Mechanics, prediction and assessment* (pp. 89-97).

1405 U.S. Forest Service, Burned Area Emergency Response, Dolan Postfire BAER Soil Burn Severity Map Released,  
1406 October 10, 2020, [https://inciweb.nwcg.gov/photos/CALPF/2020-10-06-1821-Dolan-PostFire-](https://inciweb.nwcg.gov/photos/CALPF/2020-10-06-1821-Dolan-PostFire-BAER/related_files/pict20200910-143346-0.pdf)  
1407 [BAER/related\\_files/pict20200910-143346-0.pdf](https://inciweb.nwcg.gov/photos/CALPF/2020-10-06-1821-Dolan-PostFire-BAER/related_files/pict20200910-143346-0.pdf)

1408 U.S. Forest Service, Burned Area Emergency Response, Dolan Fire Burned Area Report, October 13, 2020,  
1409 [https://inciweb.nwcg.gov/photos/CALPF/2020-10-06-1821-Dolan-PostFire-](https://inciweb.nwcg.gov/photos/CALPF/2020-10-06-1821-Dolan-PostFire-BAER/related_files/pict20200927-132609-0.pdf)  
1410 [BAER/related\\_files/pict20200927-132609-0.pdf](https://inciweb.nwcg.gov/photos/CALPF/2020-10-06-1821-Dolan-PostFire-BAER/related_files/pict20200927-132609-0.pdf)



1411 U.S. Geological Survey, Postfire Debris flow Hazards: Dolan Fire (Los Padres National Forest, CA), Landslide  
1412 Hazards Program, retrieved September 27, 2021, from  
1413 [https://landslides.usgs.gov/hazards/postfire\\_debrisflow/detail.php?objectid=312](https://landslides.usgs.gov/hazards/postfire_debrisflow/detail.php?objectid=312)

1414 Vergopolan, N., Chaney, N.W., Beck, H.E., Pan, M., Sheffield, J., Chan, S., & Wood, E.F. (2020). Combining  
1415 hyper-resolution land surface modeling with SMAP brightness temperatures to obtain 30-m soil  
1416 moisture estimates. *Remote Sensing of Environment*, 242, 111740.  
1417 doi:<https://doi.org/10.1016/j.rse.2020.111740>

1418 Wang, J., Wang, C., Rao, V., Orr, A., Yan, E., & Kotamarthi, R. (2019). A parallel workflow implementation  
1419 for PEST version 13.6 in high-performance computing for WRF-Hydro version 5.0: a case study over  
1420 the midwestern United States. *Geoscientific Model Development*, 12(8), 3523-3539. doi:10.5194/gmd-  
1421 12-3523-2019

1422 Williams, A.P., Abatzoglou, J.T., Gershunov, A., Guzman-Morales, J., Bishop, D.A., Balch, J.K., & Lettenmaier,  
1423 D.P. (2019). Observed Impacts of Anthropogenic Climate Change on Wildfire in California. *Earth's*  
1424 *Future*, 7(8), 892-910. doi:<https://doi.org/10.1029/2019EF001210>

1425 Williams, A.P. et al. (2022) Growing impact of wildfire on western US water supply. 119:e2114069119  
1426 doi:10.1073/pnas.2114069119 %J Proceedings of the National Academy of Sciences

1427 Xia, Y., Mitchell, K., Ek, M., Cosgrove, B., Sheffield, J., Luo, L., . . . Lohmann, D. (2012). Continental-scale  
1428 water and energy flux analysis and validation for North American Land Data Assimilation System  
1429 project phase 2 (NLDAS-2): 2. Validation of model-simulated streamflow. *Journal of Geophysical*  
1430 *Research: Atmospheres*, 117(D3). doi:<https://doi.org/10.1029/2011JD016051>

1431 Young AM, Skelly KT, Cordeira JM (2017) High-impact hydrologic events and atmospheric rivers in California:  
1432 An investigation using the NCEI Storm Events Database *Geophys Res Lett* 44:3393-3401  
1433 doi:10.1002/2017GL073077

1434 Yin D., Xue Z. G., Gochis D. J., Yu W., Morales M., & Rafieeiniasab A. (2020) A Process-Based, Fully  
1435 Distributed Soil Erosion and Sediment Transport Model for WRF-Hydro 12:1840

1436 Zhang, J. et al. (2011). National Mosaic and Multi-Sensor QPE (NMQ) system: Description, results, and future  
1437 plans. *Bull. Amer. Meteor. Soc.*, 92, 1321–1338, <https://doi.org/10.1175/2011BAMS-D-11-00047.1>.

1438 Zhang, J., Qi, Y., Langston, C., Kaney, B., & Howard, K. (2014). A real-time algorithm for merging radar QPEs  
1439 with rain gauge observations and orographic precipitation climatology. *J. Hydrometeor.*, 15, 1794–1809,  
1440 <https://doi.org/10.1175/JHM-D-13-0163.1>.

1441 Zhang, J. et al. (2016). Multi-Radar Multi-Sensor (MRMS) quantitative precipitation estimation: Initial  
1442 operating capabilities. *Bull. Amer. Meteor. Soc.*, 97, 621–638, <https://doi.org/10.1175/BAMS-D-14-00174.1>.

1444 Zhang S., Zhao, L., Delgado-Tellez, R., Bao, H. (2018) A physics-based probabilistic forecasting model for  
1445 rainfall-induced shallow landslides at regional scale *Nat Hazards Earth Syst Sci* 18:969-982  
1446 doi:10.5194/nhess-18-969-2018

1447 Zhu, Y., & Newell, R. E. (1998). A Proposed Algorithm for Moisture Fluxes from Atmospheric Rivers, *Monthly*  
1448 *Weather Review*, 126(3), 725-735. Retrieved May 14, 2022, from  
1449 [https://journals.ametsoc.org/view/journals/mwre/126/3/1520-0493\\_1998\\_126\\_0725\\_apafmf\\_2.0.co\\_2.xml](https://journals.ametsoc.org/view/journals/mwre/126/3/1520-0493_1998_126_0725_apafmf_2.0.co_2.xml)

1451